



Novel Fenton-like system based on bifunctional MgO/g-C₃N₄ S-scheme heterojunction photoanode for efficient tetracycline degradation

Jiangli Sun^{a,b,c}, Huizhong Wu^{a,b,c}, Chunhong Fu^{a,b,c}, Chaohui Zhang^{a,b,c}, Zhongzheng Hu^{a,b,c}, Minghua Zhou^{a,b,c,*}

^a Key Laboratory of Pollution Process and Environmental Criteria, Ministry of Education, College of Environmental Science and Engineering, Nankai University, Tianjin 300350, China

^b Tianjin Key Laboratory of Environmental Technology for Complex Trans-Media Pollution, College of Environmental Science and Engineering, Nankai University, Tianjin 300350, China

^c Tianjin Advanced Water Treatment Technology International Joint Research Center, College of Environmental Science and Engineering, Nankai University, Tianjin 300350, China

ARTICLE INFO

Keywords:

S-scheme heterojunction
Photoelectrocatalysis
H₂O₂ activation
Fenton-like
Organic pollutant

ABSTRACT

A novel photoelectrocatalytic (PEC) system consisting of S-scheme MgO/g-C₃N₄ photoanode and modified carbon felt (MCF) cathode was designed for efficient degradation of tetracycline, in which photoanode had both efficient photocatalytic performance and activation of H₂O₂ produced by the MCF cathode. After 30 min of LED irradiation, the PEC system could completely remove tetracycline at cathodic bias of −0.5 V (vs. Ag/AgCl), and the degradation rate constants were 5.3 and 1.5 times that of electrocatalysis and photocatalysis. The charge transfer mechanism of S-scheme MgO/g-C₃N₄ was verified by experimental studies and DFT calculations. Mg-N coordination was the key to activate H₂O₂ to produce singlet oxygen (¹O₂) and hydroxyl radicals ([•]OH). The PEC system had excellent degradation performance at pH ranges 4–10, which solved the bottleneck that Fenton system is effective at narrow pH range. This study provides new ideas for preparation of bifunctional photoanodes and new insights into the PEC process.

1. Introduction

Antibiotics are widely used in human therapeutics and livestock industry, which is an emerging class of organic pollutants. Tetracycline (TC) is a common broad-spectrum tetracycline antibiotic, and the level of TC in farm wastewater can be as high as approximately 20 mg L^{−1} [1, 2]. Greater than 70% of antibiotic doses are incompletely absorbed and released into the environment through urine and feces [3]. However, based on their chemical stability, TC are not easily degraded in the natural environment and pose a threat to ecosystems [4]. Therefore, there is a need to identify an efficient, energy-saving and environmentally friendly technique for TC removal.

In recent years, advanced oxidation processes (AOPs) such as photocatalysis, ozonation, electrochemical oxidation, and Fenton/Fenton-like oxidation have become effective in removing various organic pollutants from water based on their ability to generate efficient reactive oxygen species (ROSS) [5–8]. Among them, Fenton/Fenton-like

technology is one of the most widely used AOPs, which is capable of utilizing H₂O₂ to generate a variety of ROSS such as hydroxyl radicals ([•]OH) and singlet oxygen (¹O₂) and effectively remove organic pollutants. Hydrogen peroxide (H₂O₂) is a mild green oxidizing agent that has been widely used in the field of AOPs for organic pollutant degradation. However, in practice the Fenton reaction is susceptible to the limitations of narrow pH range and generation of secondary iron sludge as well as low H₂O₂ activation efficiency and utilization [9,10]. To solve the above challenges, Fenton process is coupled with photocatalytic method to form a new photoelectrocatalytic (PEC) technology that is highly efficient and less susceptible to interference from the external environment. This PEC system can effectively separate photogenerated carriers by utilizing the relatively small potential under light radiation, thus realizing the removal of organic pollutants. Meanwhile, the cathode of the PEC system produces H₂O₂ under cathodic bias and utilizes it in-situ for wastewater purification. Therefore, it is critical to design a bifunctional anode with efficient photocatalytic properties and simultaneous

* Corresponding author at: Key Laboratory of Pollution Process and Environmental Criteria, Ministry of Education, College of Environmental Science and Engineering, Nankai University, Tianjin 300350, China.

E-mail address: zhoumh@nankai.edu.cn (M. Zhou).

<https://doi.org/10.1016/j.apcatb.2024.123976>

Received 5 February 2024; Received in revised form 10 March 2024; Accepted 17 March 2024

Available online 18 March 2024

0926-3373/© 2024 Elsevier B.V. All rights reserved.

activation of H_2O_2 generated from the cathode.

In recent years, the proposal of S-scheme heterojunction photocatalysts has been recognized and applied by a wide range of scholars. Compared with the conventional heterojunction, the S-scheme heterojunction realizes the effective separation of e^- - h^+ pairs and endows the composites with superb redox capacity under the internal electric field, band edge bending and Coulomb interaction [11]. Among them, the S-scheme heterojunction formed by an organic-inorganic semiconductor combines the advantages of the two semiconductors, making it one of the best solutions for constructing S-scheme heterojunctions [12]. Inorganic semiconductors produce photogenerated carriers after absorbing light energy which are easy to separate, such as WO_3 , BiVO_4 , and TiO_2 . Based on the limited variety of inorganic semiconductors, the development of new photocatalysts is restricted. However, organic semiconductors have greater functionality. Therefore, the organic-inorganic semiconductor S-scheme heterojunction with strong redox ability is constructed. For example, Sun et al. developed a $\text{g-C}_3\text{N}_4/\text{WO}_3/\text{ZnS}$ double S-type heterojunction that degraded 85% of tetracycline within 1 h of summer light and had the potential to degrade TC in different matrix water sources under natural light [13]. Wang et al. synthesized $\text{g-C}_3\text{N}_4/\text{TiO}_2$ S-scheme photocatalysts by electrostatic spinning and calcination and used them for the removal of Congo Red. The apparent reaction rate constants of $\text{g-C}_3\text{N}_4/\text{TiO}_2$ were 3.4 and 8.2 times that of bare TiO_2 and $\text{g-C}_3\text{N}_4$, respectively [14].

Graphitic carbon nitride ($\text{g-C}_3\text{N}_4$) has attracted much attention for its excellent chemical stability, moderate band gap and good visible light responsivity [15,16]. In addition, $\text{g-C}_3\text{N}_4$ has unique electronic properties can act as an electron donor and reduce the leaching of metal ions [17]. However, the fast photogenerated carrier complexation rate of $\text{g-C}_3\text{N}_4$ limits its application. Therefore, a co-catalyst is needed to combine with $\text{g-C}_3\text{N}_4$ to form a heterojunction to reduce the carrier complexation rate and enhance the photocatalytic performance. Magnesium oxide (MgO) is an inexpensive, non-toxic photocatalyst with a high specific surface and unique chemical properties [18,19]. However, MgO with a wide band gap can only respond to ultraviolet light. Therefore, effective bonding of MgO to $\text{g-C}_3\text{N}_4$ to construct an S-scheme heterojunction can not only enhance the light absorption range of MgO , but also inhibit the complexation of photogenerated carriers, thus enhancing the photocatalytic activity [20]. For example, Gao et al. constructed $\text{MgO/g-C}_3\text{N}_4$ S-scheme photocatalyst by liquid deposition and calcination [21]. The degradation of Rhodamine B (100 mg L^{-1}) by photo-Fenton was tested under the condition of additional H_2O_2 . $\text{MgO/g-C}_3\text{N}_4$ photo-Fenton degradation activity (80.01%) on Rhodamine B was higher than that of $\text{g-C}_3\text{N}_4$ (28.46%) and MgO (55.64%), under 300 W Xe lamp irradiation. Therefore, the activation performance of S-scheme $\text{MgO/g-C}_3\text{N}_4$ photoanode can be further improved by simplifying the preparation strategy and PEC system construction, and it can be loaded on the substrate to improve the recovery efficiency. In addition, the MgNCN/MgO composite prepared by Ge et al. had excellent Fenton-like catalytic performance, which was mainly attributed to the Mg-N coordination between MgO and MgNCN [20]. At the same time, it was reported that carbon black modified carbon felt (MCF) was a cost-effective cathode to produce H_2O_2 [20]. Therefore, this $\text{MgO/g-C}_3\text{N}_4$ photoanode would be available as a bifunctional bridge connecting activated H_2O_2 and photocatalytic process to degrade organic pollutants, however, it has not been attempted.

Herein, in this study, the PEC system consisting of $\text{MgO/g-C}_3\text{N}_4$ S-scheme heterojunction photoanode and MCF cathode was constructed to enhance photocatalytic activity and solve the pH limitation in Fenton reaction. $\text{MgO/g-C}_3\text{N}_4$ S-scheme heterojunction photoanode and MCF cathode was prepared by one-step calcination method and used for PEC to degrade TC efficiently. The PEC system could degrade organic pollutant under actual sunlight or LED light irradiation. This PEC system had higher activity against organic pollutants compared to photocatalytic (PC) and electrocatalytic (EC) systems. In addition, comparative experiments of TC degradation by different systems as well as

density functional theory (DFT) calculations were performed to determine the activation effect of $\text{MgO/g-C}_3\text{N}_4$ on the H_2O_2 produced at the cathode. Furthermore, *in-situ* irradiation XPS and DFT calculations verified that $\text{MgO/g-C}_3\text{N}_4$ efficiently carriers transfer and separate consistent with S-scheme heterojunctions. Finally, the environmental suitability and stability of the PEC system as well as the toxicity of the degradation intermediates of TC were evaluated. This study provides ideas for the construction of a Fenton-like system for the efficient degradation of organic pollutants by dual-function S-scheme heterojunction photoanodes.

2. Experimental section

2.1. Materials

All the chemicals were of analytical grade. Deionized water was used throughout this study. Basic magnesium carbonate pentahydrate ($(\text{MgCO}_3)_4\cdot\text{Mg}(\text{OH})_2\cdot 5\text{H}_2\text{O}$), melamine ($\text{C}_3\text{H}_6\text{N}_6$), sodium sulfate (Na_2SO_4), sulfuric acid (H_2SO_4 , 95–98 wt%) and tetracycline (TC) were purchased from Aladdin Chemical Reagent Co., Ltd. Both carbon black (VXC72R) and polytetrafluoroethylene (PTFE) were bought from Shanghai Hesens Electric Co., Ltd. The carbon felt (CF) was bought from Jinglong Co., Ltd.

2.2. Electrodes preparation

2.2.1. Preparation of photoanodes

Typically, alkaline magnesium carbonate and melamine were ground in a mortar in a mass ratio of 1:2 for 30 min. The homogeneous mixture was placed in a crucible with a lid and sealed with aluminum foil, after which the crucible was placed in a muffle furnace and kept at 550°C for 120 min. The $\text{MgO/g-C}_3\text{N}_4$ photocatalyst was obtained by naturally cooling to room temperature and grinding again with a mortar and pestle to a uniform powder. The obtained $\text{MgO/g-C}_3\text{N}_4$ powder was homogeneously mixed with ethanol and Nafion solution. Wherein the loading amount of $\text{MgO/g-C}_3\text{N}_4$ photocatalyst on the fluorine-doped tin oxide-coated (FTO) glasses ($4 \text{ cm} \times 2 \text{ cm}$) was 3 mg cm^{-2} , and the volume ratio of ethanol to Nafion solution was 6:1. The mixture was coated on the FTO substrate to obtain the $\text{MgO/g-C}_3\text{N}_4$ photoanode. Similarly, $\text{g-C}_3\text{N}_4$ and MgO photoanodes were obtained without the addition of basic magnesium carbonate or melamine.

2.2.2. Preparation of MCF cathode

The obtained MCF were mixed with 0.13 g carbon black, 0.93 mL ethanol, 0.93 mL deionized water and 0.24 mL polytetrafluoroethylene (PTFE), and then the mixture was shock-dispersed and applied to a clean carbon felt of the same area as the FTO. After drying at room temperature, the MCF was placed in a muffle furnace at 360°C and annealed for 30 min to obtain the cathode material [10,22].

2.3. Characterizations

The phase structure, functional groups and chemical composition of as-prepared MgO , $\text{g-C}_3\text{N}_4$ and $\text{MgO/g-C}_3\text{N}_4$ catalysts were characterized by X-ray diffraction (XRD, Ulitima IV, Japan), the Fourier transform infrared (FTIR, TENSOR 37 spectrometer, Germany) spectra and the X-ray photoelectron spectroscopy (XPS, Thermo Scientific ESCALAB 250Xi, USA). The morphology and microstructure of the electrodes were investigated by the field-emission scanning electron microscopy (FESEM, Sigma-300, Germany), transmission electron microscopy (TEM, JEM-2100, Japan) equipped with the energy-dispersive X-ray spectroscopy (EDS) and high-resolution TEM (HRTEM). The Brunauer-Emmett-Teller (BET) specific surface area was investigated on ASAP 2460 instrument (ASAP 2460, USA). Optical absorption properties were detected by the UV-vis diffuse reflectance spectrum (UV-vis DRS, UV-2600, Japan). The photoluminescence (PL, F7000, Japan) spectrum

was conducted to characterize the optical properties at excitation wavelength of 360 nm. The time resolved photoluminescence (TRPL, FLS1000, The United Kingdom) were examined to get fluorescence lifetimes of photogenerated carriers.

2.4. Degradation experiments and analytical methods

The performance of the photoanode for H_2O_2 activation and pollutant degradation were evaluated by using TC as a model organic pollutant. The prepared photoanode was employed as the anode and MCF as the cathode, and the light source was actual sunlight or LED lamp ($380\text{ nm} < \lambda < 840\text{ nm}$). Experiments were conducted on a single chamber quartz reactor with a contaminant TC concentration of 20 mg L^{-1} and an electrolyte of $0.1\text{ M Na}_2\text{SO}_4$ solution. The experimental conditions of EC and PC were consistent with PEC except no light source or no applied voltage.

The concentration of TC was determined by high-performance liquid chromatography (HPLC, Ultimate 3000 ThermoFisher, USA) with a C18 column at 30°C at wavelength of 355 nm . Mobile phase was acetonitrile and water at 18:82 with a flow rate of 0.5 mL min^{-1} . The generated H_2O_2 concentration was evaluated by UV-vis spectrophotometer (UV835, Shanghai Lab-Spectrum Instrument Co., Ltd.) according to the method of potassium titanium (IV) oxalate at 400 nm [23]. The degradation intermediates of TC in this system were identified by liquid chromatography coupled with a mass spectrometry (LC-MS, Orbitrap Fusion, Thermo, USA). The mobile phase was acetonitrile/water (80/20, v/v) and the flow rate of 0.4 mL min^{-1} [24].

To identify the dominant reactive species towards contaminants removals, ammonium oxalate (AO), tert-Butanol (TBA), 1,4-benzoquinone (BQ) and furfuryl alcohol (FFA) were used as scavengers for h^+ , $\cdot\text{OH}$, $\text{O}_2^{\cdot-}$ and $^1\text{O}_2$, respectively, at a concentration of 50 mM . The generated active species ($\cdot\text{OH}$, $\text{O}_2^{\cdot-}$ and $^1\text{O}_2$) were determined by the electron paramagnetic resonance (EPR) spectrometer (Bruker EMX Nano, Germany) with 5,5-dimethyl-pyrroline N-oxide (DMPO) and 2,2,6,6-tetramethyl-4-piperidinol (TEMP) as the spin-trapper agent, respectively.

2.5. Photoelectrochemical measurements

The photoelectrochemical measurements were tested in a three-electrode cell using an electrochemical analyzer (CHI 760E, Chenhua, Shanghai, China). The prepared photoanodes, Pt foil and Ag/AgCl electrode were used as working electrodes, counter electrodes and reference electrode, respectively. The electrolyte was Na_2SO_4 aqueous solution (0.1 M). The electrochemical impedance spectroscopy (EIS) and Mott-Schottky curves (MS) were carried out using an electrochemical workstation (CHI 760E, Chenhua, Shanghai, China). Transient photocurrent responses were obtained with a 50 W LED lamp (China, XC-50W1A5-OSP) as the light source, with the light density parameter was 0.142 W cm^{-2} .

2.6. DFT calculations

First-principles calculations were completed by the Vienna ab initio simulation package (VASP 5.4.1) using the Perdew-Burke-Ernzerhof (PBE) method [25–27]. In the framework of the projective augmented wave method, the cutoff energy of the plane wave basis was set to 400 eV . Besides, a $3 \times 3 \times 1$ Monkhorst-pack grid was employed. All the structures were converged to 0.01 eV/\AA .

3. Results and discussion

3.1. Structure and morphology of photoelectrodes

$\text{MgO/g-C}_3\text{N}_4$ composites were synthesized by one-step calcination method. The microstructure and morphology of the samples were analyzed using SEM, TEM and EDS. As shown in Fig. 1a, the disordered MgO nanoparticles with the size of $40\text{--}100\text{ nm}$ (Fig. S1a-b) were distributed on the stacked irregular $\text{g-C}_3\text{N}_4$ nanosheets, which was due to the nucleation and growth of MgO particles. Similarly, it could be shown by TEM images (Fig. 1b) that the $\text{g-C}_3\text{N}_4$ nanosheets with grown MgO particles were much rougher than the pristine $\text{g-C}_3\text{N}_4$ nanosheets (Fig. S1c-d). The HRTEM image (Fig. 1c) showed an interplanar spacing of 0.211 nm in the $\text{MgO/g-C}_3\text{N}_4$ composite, corresponding to the (200) plane of the MgO [28]. In addition, the elemental mapping displayed

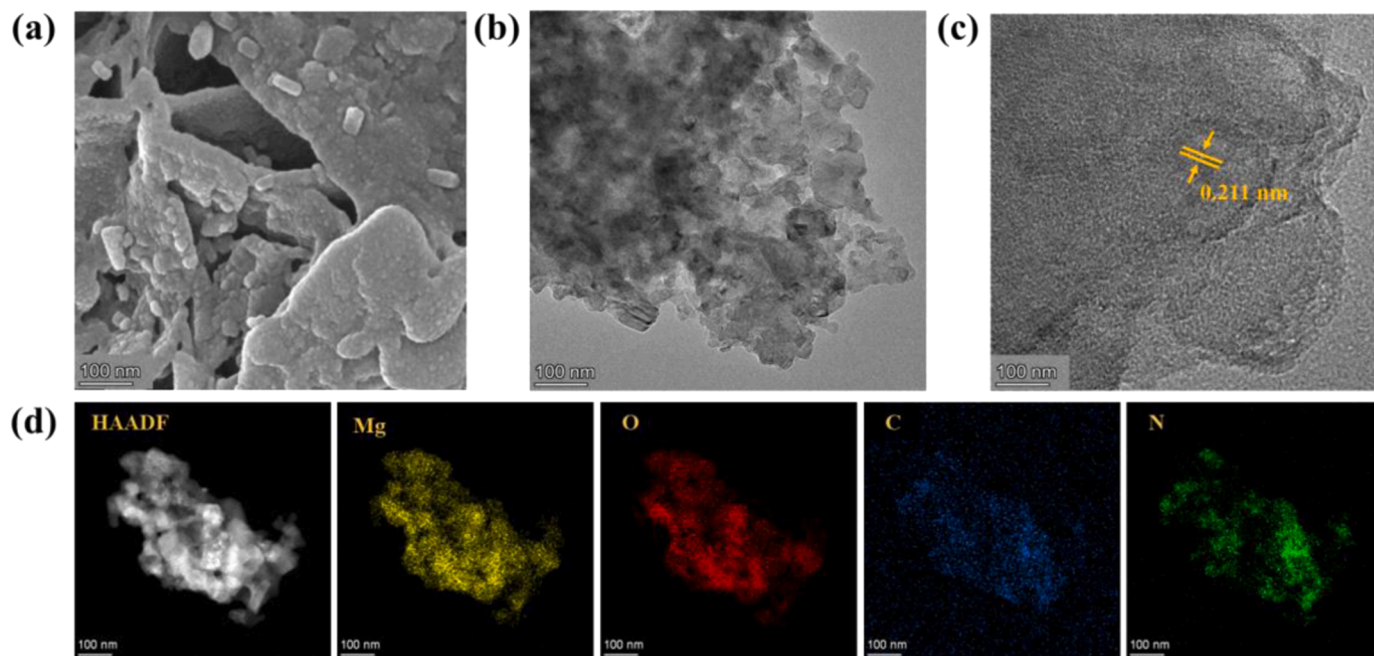


Fig. 1. (a) SEM image of $\text{MgO/g-C}_3\text{N}_4$; (b) TEM image of $\text{MgO/g-C}_3\text{N}_4$; (c) HRTEM image of $\text{MgO/g-C}_3\text{N}_4$; (d) Elemental mapping of Mg, O, C, and N of $\text{MgO/g-C}_3\text{N}_4$ (TEM-EDS).

that the Mg, O, C, and N elements were uniformly distributed in the g-C₃N₄ composites (Fig. 1d).

The crystalline phase structures of g-C₃N₄, MgO and MgO/g-C₃N₄ samples were investigated by XRD. Fig. 2a showed that the diffraction peaks of MgO were located at $2\theta = 37.0^\circ, 42.9^\circ, 62.3^\circ, 74.7^\circ$ and 78.7° , derived from the (111), (200), (220), (311) and (222) planes of MgO with a periclase structure (JCPDS 01-087-0651) [29]. The g-C₃N₄ showed two characteristic peaks at $2\theta = 13.0^\circ$ and 27.4° , which were well ascribed to the (100) and (002) planes, respectively (JCPDS 87-1526) [30]. For the MgO/g-C₃N₄ composites, in addition to the MgO diffraction peaks, there were diffraction peaks with $2\theta = 18.9^\circ, 34.1^\circ, 45.3^\circ, 56.3^\circ$ and 67.3° from the (003), (012), (015), (110) and (202) plane (JCPDS 00-051-0540) of MgNCN with rhombohedral structure [20]. This could be attributed to the interaction between MgO and g-C₃N₄ nanosheets.

Subsequently, the functional groups of the samples and the interactions between the catalysts were investigated by the FTIR spectra in Fig. 2b. The g-C₃N₄ had obvious characteristic peaks in the region of $1200\text{--}1700\text{ cm}^{-1}$, which belonged to the typical C=N stretching vibration and C-N heterocyclic vibration [30]. The characteristic peaks of g-C₃N₄ in the MgO/g-C₃N₄ composites were obviously weakened, which was attributed to the interaction between MgO and g-C₃N₄. The peak at 1640 cm^{-1} was weaker than the individual g-C₃N₄ peaks, attributed to the coordination of the Mg atoms in MgO and the N atoms in g-C₃N₄. In addition, the peak at 487 cm^{-1} belonged to the vibration of the Mg-O bond [31]. Two new characteristic adsorption peak positions at 2140 and 675 cm^{-1} were added in the MgO/g-C₃N₄ composites, attributed to the stretching vibration and deformation vibration of N-C-N [32]. The existence of Mg-N bond in MgO/g-C₃N₄ composites was further explained.

The surface chemical composition and state of the catalysts were further investigated by XPS measurements. As shown in Fig. 3a, all elements with g-C₃N₄ and MgO inside the composite could be detected in the XPS survey spectra. The high-resolution Mg 1s spectrum of the MgO/g-C₃N₄ composites (Fig. 3b) showed two more peaks than MgO, which were attributed to the N-Mg-N bond (1303.13 eV) and the N-Mg-O bond (1303.71 eV), suggesting that interactions between MgO and g-C₃N₄ had occurred. In addition, the peak at 1304.30 eV corresponded to the O-Mg-O bond. The peak at 530.24 eV in the high-resolution O 1s XPS spectrum of MgO/g-C₃N₄ composites (Fig. 3c) corresponded to the C-O bond, meanwhile, the two peaks at 531.63 eV and 532.90 eV were attributed to the lattice oxygen and adsorbed oxygen of MgO. As shown in Fig. 3d, the high-resolution C 1s XPS spectra of MgO/g-C₃N₄ composites displayed peaks at 286.77 eV and 289.57 eV , which belonged to C-O bonds and carbonates [31]. Additionally, there was a peak of 285.00 eV attributed to the N=C=N bond. The N 1s XPS spectrum (Fig. 3e) of MgO/g-C₃N₄ could be back-deconvoluted into four peaks originating from the hybridized nitrogen (C-N=C, 397.89 eV),

the tertiary nitrogen (N-(C)₃, 398.95 eV) and the amino functional groups (C-N-H, 400.44 eV) [33]. Clearly, a new peak at 397.34 eV corresponded to the Mg-N bond [28].

In addition, both *ex-situ* and *in-situ* irradiation XPS measurements were performed, and *in-situ* irradiation XPS spectroscopy is one of the effective means to study the direction of electron flow in photocatalytic heterojunctions [5]. It can be well observed from the *ex-situ* XPS spectra that the Mg 1s and O 1s bonding in the MgO/g-C₃N₄ composites could be shifted in a lower direction (Fig. 3b-c), while the C 1s and N 1s bonding could be shifted in a higher direction (Fig. 3d-e), compared to the pure g-C₃N₄ and MgO. The above shifts in the binding energies indicated that electrons were transferred from g-C₃N₄ to MgO after hybridization due to the different work functions of the two semiconductors. At the same time, the electron transfer created an internal electric field at the interface between g-C₃N₄ and MgO, which was directed from g-C₃N₄ towards MgO. Furthermore, this indicated the existence of g-C₃N₄ upward energy band bending and MgO downward energy band bending at the MgO/g-C₃N₄ heterojunction interface. In addition, *in-situ* irradiation XPS measurements of MgO/g-C₃N₄ showed that Mg 1s and O 1s binding could significantly move to higher energy levels, while C 1s and N 1s binding could significantly move to lower energy levels, compared to XPS without photoexcitation. Driven by the internal electric field and the bending energy band, photoelectrons in the conduction band of MgO spontaneously transferred to g-C₃N₄ and combined with holes in the VB of g-C₃N₄ under light irradiation [34]. Thus, the XPS results provided important evidence for the carrier transfer pathway at the MgO/g-C₃N₄ heterojunction interface under light irradiation. Among them, the migration of photogenerated electrons from MgO to g-C₃N₄ is consistent with the S-scheme mechanism.

The surface redox reactions of MgO/g-C₃N₄ in the PEC system was closely related to its surface area and active sites. Therefore, the N₂ adsorption-desorption isotherm for g-C₃N₄, MgO and MgO/g-C₃N₄ with pore size distribution was shown in Fig. 3f. All catalysts were IV-type isotherms and H3 hysteresis loops, indicating the presence of mesopores in the catalysts [14]. Furthermore, the Brunauer-Emmett-Teller surface area of g-C₃N₄ and MgO were 13.47 and $66.84\text{ cm}^2\text{ g}^{-1}$, respectively, as shown in Table S1. The surface area of MgO/g-C₃N₄ ($16.35\text{ cm}^2\text{ g}^{-1}$) was less than the pure MgO due to the lower specific surface area of g-C₃N₄. Compared with pure g-C₃N₄, the introduction of MgO improved the specific surface area, pore volume and pore size of MgO/g-C₃N₄. Particularly, the nanoparticles with higher surface area will provide a large number of active sites, which is favorable for the improvement of catalytic performance.

3.2. Photoelectrochemical characterization of different photoanodes

The light absorption properties of g-C₃N₄, MgO and MgO/g-C₃N₄ were investigated using UV-vis DRS, as shown in Fig. 4a. The light

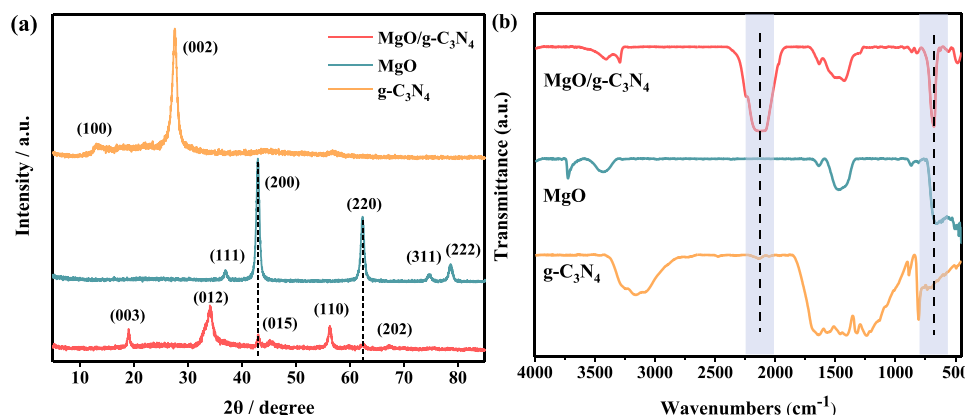


Fig. 2. (a) XRD patterns and (b) FTIR spectra of g-C₃N₄, MgO and MgO/g-C₃N₄.

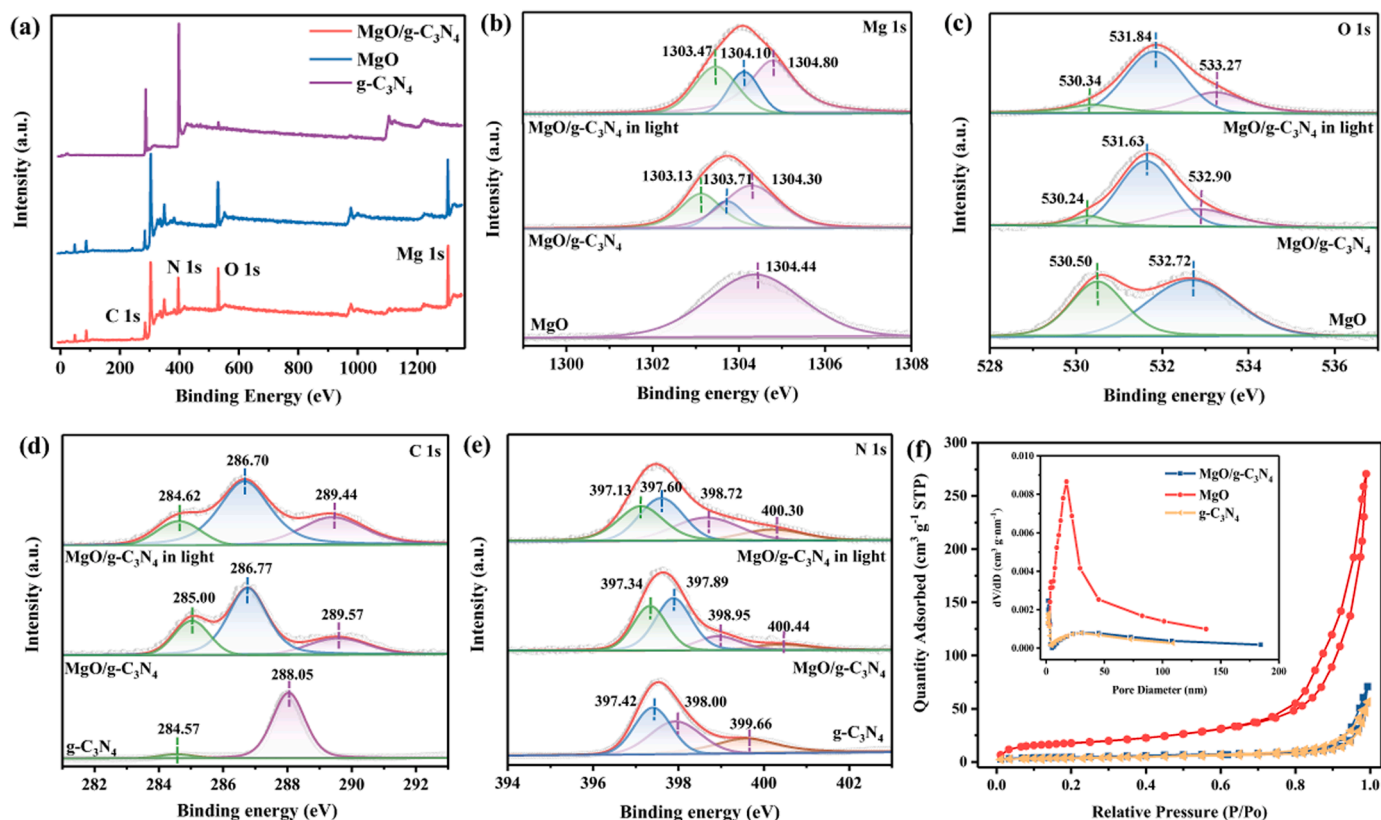


Fig. 3. (a) XPS survey spectra of g-C₃N₄, MgO and MgO/g-C₃N₄; *ex-situ/in-situ* irradiated XPS spectra of (b) Mg 1s, (c) O 1s, (d) C 1s, (e) N 1s; (f) N₂ adsorption-desorption isotherm for g-C₃N₄, MgO and MgO/g-C₃N₄ with pore size distribution (inset).

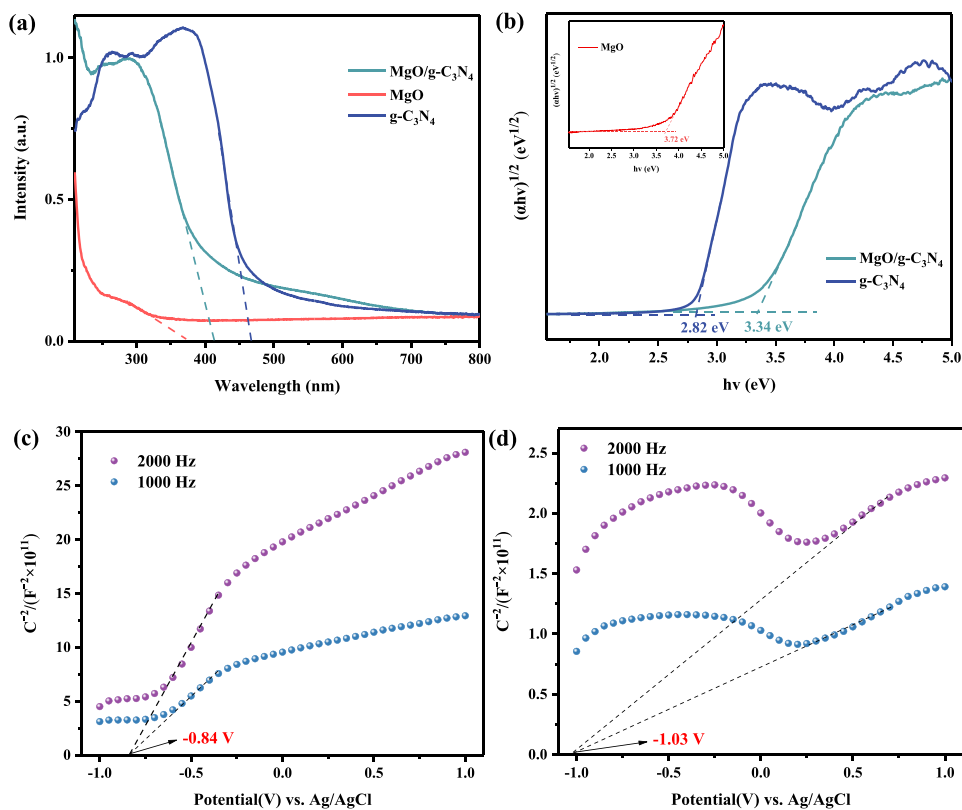


Fig. 4. (a) UV-vis DRS spectra of different photoelectrodes; (b) band gaps and Mott-Schottky plots of (c) MgO and (d) g-C₃N₄.

absorption edge of pure MgO was around 370 nm, which could be attributed to its wider band gap. While g-C₃N₄ had a better visible light absorption property in the light absorption range of about 200–465 nm. In addition, the MgO/g-C₃N₄ composites had an absorption edge of about 420 nm due to the presence of g-C₃N₄, indicating that the composites could harvest visible light more efficiently. As shown in Fig. 4b, the band gaps of different catalysts were calculated using the UV–vis DRS results, and the more detailed band gap energy values were estimated to be 2.82, 3.72 and 3.34 eV for g-C₃N₄, MgO and MgO/g-C₃N₄, respectively. The band gaps of the MgO/g-C₃N₄ were reduced as compared to that of g-C₃N₄. The narrower bandgap was more favorable for photogenerated electron leaps, indicating that MgO/g-C₃N₄ was more susceptible to photoexcitation and electron-hole separation [35].

The Mott-Schottky test determined the type of semiconductor and the corresponding flat-band potential, as shown in Fig. 4c and 4d. The Mott-Schottky plots for both MgO and g-C₃N₄ displayed positive slopes, suggesting n-type properties. By linear fitting, the flat-band potentials of MgO and g-C₃N₄ were calculated to be −0.64 eV (vs. NHE) and −0.83 eV (vs. NHE), respectively. For n-type semiconductors, the difference between the conduction band (CB) potential and the flat band potential is about negative 0.1 V [8]. Therefore, the CB potentials of MgO and g-C₃N₄ were calculated to be about −0.74 eV (vs. NHE) and −0.93 eV (vs. NHE), respectively. Subsequently, according to the equation $E_{VB} = E_{CB} + E_g$ (vs. NHE), combined with the MgO (3.72 eV) and g-C₃N₄ (2.82 eV) band gap energies, the valence band (VB) potential could be estimated to be 2.98 eV (vs. NHE) and 1.89 eV (vs. NHE), respectively [36,37].

Photoluminescence tests were performed on different photoanodes to investigate the separation efficiency of photogenerated electron-hole pairs. The lower intensity of PL indicates the lower rate of carrier recombination in the catalysts [38]. The PL emission spectra of g-C₃N₄, MgO and MgO/g-C₃N₄ were obtained at an excitation wavelength of 380 nm (Fig. 5a). The results showed that the PL intensity of MgO/g-C₃N₄ was significantly reduced compared to that of g-C₃N₄,

revealing the effectiveness of the heterojunction in suppressing the photogenerated carrier complexation.

In addition, time-resolved fluorescence (TRPL) decay spectroscopy was performed to understand the carrier separation behavior, and the curves were fitted to three-exponential. The fluorescence decay profiles of g-C₃N₄, MgO and MgO/g-C₃N₄ were measured under 365 nm excitation. The fitted τ_1 (slow decay time), τ_2 and τ_3 (fast decay time) as well as τ_{av} (average lifetimes) were shown in Fig. 5b. The lifetimes about τ_1 , τ_2 and τ_3 of MgO/g-C₃N₄ were between g-C₃N₄ and MgO, respectively, which may be due to the composite of g-C₃N₄ and MgO [39]. The calculated average lifetimes of g-C₃N₄, MgO and MgO/g-C₃N₄ were 23.73, 6.20 and 5.67 ns, respectively (Table S2). Furthermore, the average lifetimes of MgO/g-C₃N₄ were 3–4 times shorter than those of the original g-C₃N₄ and MgO. The shorter average lifetimes of MgO/g-C₃N₄ indicated the emergence of a non-radiative pathway, where more carriers were separated to the solid-liquid interface, thus accelerating the photocatalytic degradation of organic matter [40,41].

The photoelectron-chemical responses were recorded under intermittent light. As shown in Fig. 5c, the photocurrent intensity exhibited a sharp rise and fall with the on/off cycle of the LED lamp, indicating that photogenerated electrons were produced at the photoanode under light illumination. Usually, the photocurrent intensity is positively correlated with the separation efficiency of photogenerated carriers in the photoanode. Therefore, the MgO/g-C₃N₄ photoanode exhibited the maximum photocurrent density compared with pure g-C₃N₄ and MgO, indicating a faster separation and migration efficiency of photogenerated carriers at its interface. In addition, the interfacial charge transfer behavior at different photoanodes was further recorded using EIS, as shown in Fig. 5d. When g-C₃N₄ and MgO were used as control samples, the semicircle radius of the MgO/g-C₃N₄ EIS Nyquist plot was the smallest, implying that the heterostructure could effectively reduce the charge transfer resistance. Interestingly, the semicircle radius of the EIS Nyquist plots in the light condition was significantly smaller than that in the non-illuminated condition, suggesting that light could effectively reduce the

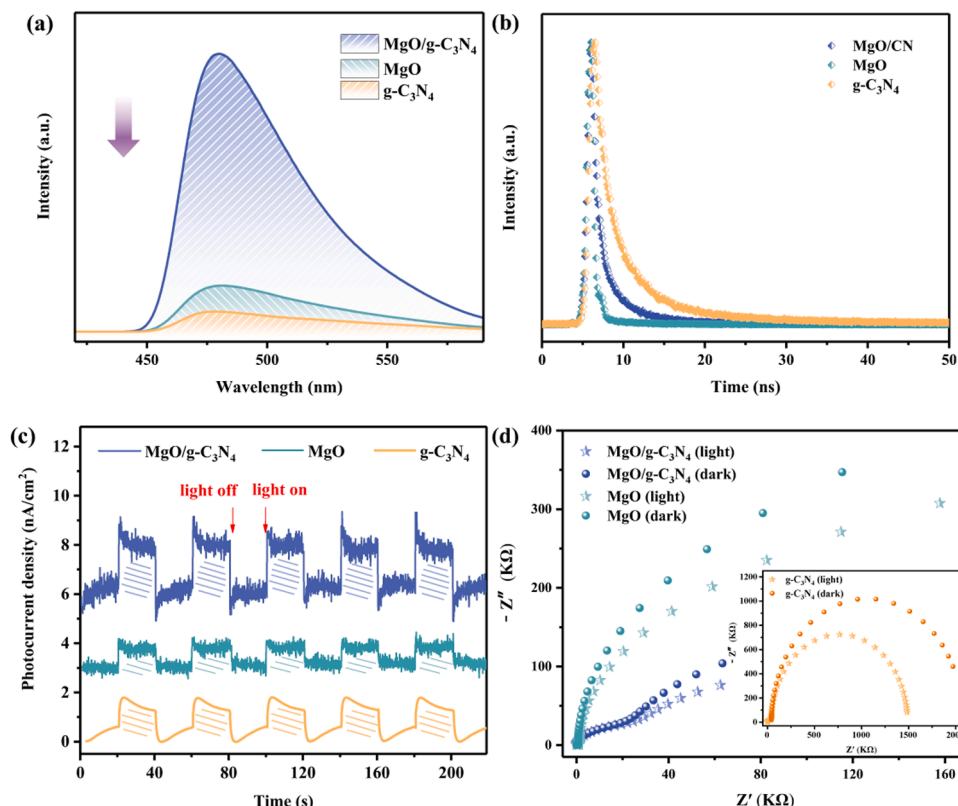


Fig. 5. (a) PL spectra, (b) TRPL spectra, (c) transient photocurrent responses, (d) EIS spectra of the as-prepared samples.

charge transfer resistance [42]. As a result, the MgO/g-C₃N₄ PEC system had superior charge transfer and separation capabilities to effectively achieve pollutant removal.

3.3. PEC activity towards H₂O₂ activation and pollutant degradation

3.3.1. Production and activation of H₂O₂ in electrocatalytic system

To explore the effects of H₂O₂ generation and activation on TC removal, the EC-ORR process was carried out in a single-compartment system. Based on the speculation that MgO/g-C₃N₄ anode can activate H₂O₂, Pt was chosen as the anode to explore the H₂O₂ yield in Pt-coupled MCF cathode system. The H₂O₂ production at the cathode for the Pt anode-coupled MCF cathode system at different cathode bias was shown in Fig. S2. Apparently, the MCF cathode produces negligible H₂O₂ at cathode bias voltages of −0.40 V and −0.45 V, probably due to the unsatisfied potential for ORR to produce H₂O₂. As the cathode bias was increased to −0.50 V and −0.55 V, the H₂O₂ production could reach 10.19 mg L^{−1} and 13.52 mg L^{−1}, respectively. It was concluded that the H₂O₂ yield increased with the increase of cathode bias. Fig. 6a showed the EC degradation efficiency of the MgO/g-C₃N₄ anode-coupled MCF cathode system under different cathode bias, and the TC degradation kinetics were fitted with the pseudo-first-order equation. More specifically, when the MCF cathode was biased at −0.40 V, the TC removal were 31.39%. The degradation of TC increased with the increase of cathode bias. The TC degradation reached 56.18% when the cathode bias was increased to −0.5 V. It can be clearly observed that the degradation efficiency of TC was proportional to the H₂O₂ yield through Fig. 6a and Fig. S2. Notably, the MgO/g-C₃N₄ anode potential was 2.35 V at a cathode bias of −0.55 V. Therefore, the cathode bias of −0.5 V was chosen as the research condition for the subsequent EC and PEC systems, taking into account the cathode-anode coupling effect and the stability of the electrodes.

In order to investigate the activation of MCF-generated H₂O₂ by

MgO/g-C₃N₄ anode, the efficiency of TC removal by EC with different anode effects was compared in the absence of light (Fig. 6b). Notably, the EC degradation efficiency of the MgO/g-C₃N₄ coupled MCF system for TC was 56.18%, which was much higher than that of the systems of g-C₃N₄ (10.13%) and MgO (37.78%), after 30 min of reaction. As shown in Fig. 6c, compared with the H₂O₂ yield in the EC system with Pt anode coupled with MCF cathode (EC-Pt-MCF, 10.19 mg L^{−1}), the remaining H₂O₂ in the EC-MgO/g-C₃N₄-MCF system was 5.83 mg L^{−1}. It was much lower than the residual H₂O₂ in the EC-g-C₃N₄-MCF (9.44 mg L^{−1}) and EC-MgO-MCF (9.35 mg L^{−1}) systems. The above results showed that the performance of TC degradation in EC system with different anodes was consistent with the trend of H₂O₂ consumption. Meanwhile, this strongly demonstrated that bonding (Mg–N) between MgO and g-C₃N₄ in MgO/g-C₃N₄ composites played an important role in EC degradation of TC. For the MgO/g-C₃N₄ anode-coupled Pt cathode system without H₂O₂ generation, the TC degradation efficiency only reached 19.68%, indicating that the EC system without H₂O₂ generation could not remove TC effectively. Secondly, the degradation efficiency of TC in the Pt anode-coupled MCF system was 19.70%, revealing that in the absence of MgO/g-C₃N₄ anode, only H₂O₂ also failed to degrade TC efficiently, which suggested that the MgO/g-C₃N₄ anode was essential for the degradation of TC. The difference between the remaining amount of H₂O₂ in the Pt anode-coupled MCF system under illumination (EC-Pt-MCF-light, 9.26 mg L^{−1}) and the production amount of the EC-Pt-MCF system (10.19 mg L^{−1}) could be ignored (Fig. 6c). This showed that LED lighting cannot effectively activate H₂O₂. The present results were interpreted as the MgO/g-C₃N₄ anode effectively utilized and activated H₂O₂ under light irradiation-independent conditions, while generating more ROS to enhance the TC degradation efficiency, which may be due to the Mg–N coordination between MgO and g-C₃N₄ to form an electron-rich N center.

In addition, the optimized models for the adsorption of H₂O₂ molecules on MgO, g-C₃N₄ and MgO/g-C₃N₄ were compared, as shown in

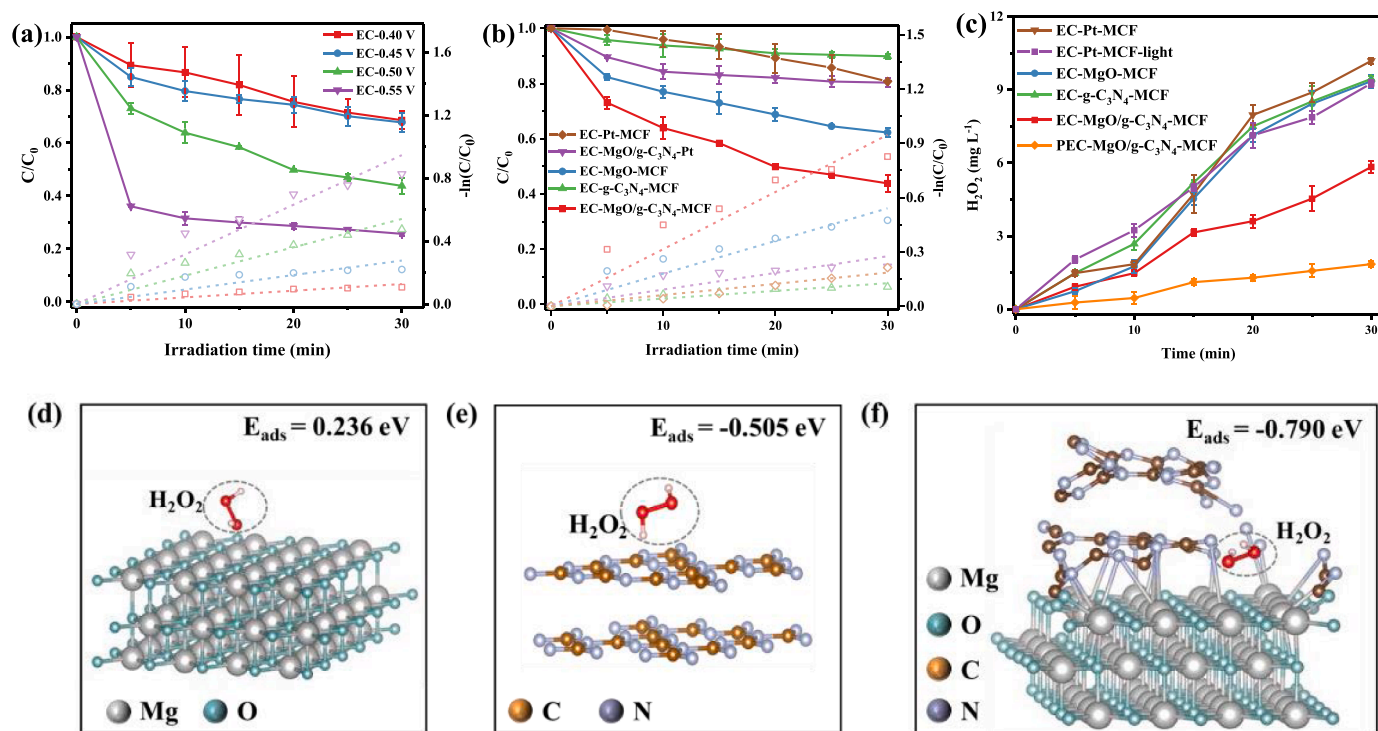


Fig. 6. (a) Degradation rate and pseudo-first-order kinetic curves of TC under different cathode bias in MgO/g-C₃N₄ anode coupled MCF cathode system, (b) degradation rate and pseudo-first-order kinetic curves of TC in different EC systems, (c) Production or remaining amount of H₂O₂ in different systems. Experimental conditions: initial TC concentration = 20 mg L^{−1}, Na₂SO₄ concentration = 0.1 M, pH = 5.6, cathode bias = 0.5 V. (d-f) Adsorption energy of H₂O₂ on MgO (200), g-C₃N₄ (002) and MgO/g-C₃N₄.

Fig. 6d-f. Obviously, the adsorption energy of H_2O_2 on $\text{MgO/g-C}_3\text{N}_4$ (-0.790 eV) was more negative than that on $\text{g-C}_3\text{N}_4$ (-0.505 eV) and MgO (0.236 eV), suggesting that the adsorption of H_2O_2 on $\text{MgO/g-C}_3\text{N}_4$ was more stable. The above study proved that $\text{MgO/g-C}_3\text{N}_4$ was more favorable for H_2O_2 adsorption.

3.3.2. Photocatalytic performance for TC oxidation

In addition, the PC performance of the $\text{MgO/g-C}_3\text{N}_4$ photoelectrode under actual sunlight and LED lamp irradiation was investigated. As shown in Fig. 7a, TC degradation was negligible under LED irradiation, indicating that TC was not easily photodegraded. In addition, the removal efficiency of TC by MgO , $\text{g-C}_3\text{N}_4$ and $\text{MgO/g-C}_3\text{N}_4$ were 89.75%, 13.25% and 96.75%, after 30 min of irradiation with LED light. Curve fitting revealed that $-\ln(C/C_0)$ was linear with irradiation time (Fig. 7b), and the degradation rate of TC was consistent with pseudo-first-order kinetics. The degradation rate constant of the $\text{MgO/g-C}_3\text{N}_4$ ($k = 0.1142 \text{ min}^{-1}$) composite catalyst was 1.6 and 20.8 times that of MgO ($k = 0.0724 \text{ min}^{-1}$) and $\text{g-C}_3\text{N}_4$ ($k = 0.0055 \text{ min}^{-1}$), respectively. In addition, pure MgO also had high TC degradation performance of PC, possibly because MgO had the ability to oxidize TC due to its suitable band gap. Since the VB potential of MgO ($E_{\text{VB}} = 2.98 \text{ eV}$) was greater than $\text{H}_2\text{O}/\text{OH}^\cdot$ potential (2.34 eV vs NHE), OH^\cdot could be generated on the VB of MgO , participating in TC degradation. Moreover, MgO ($E_{\text{CB}} = -0.74 \text{ eV}$) had more negative CB edge than $\text{O}_2/\text{O}_2^{\cdot-}$ (-0.33 eV vs NHE), hence, the electrons generated on the CB of MgO could reduce O_2 to $\text{O}_2^{\cdot-}$. Therefore, MgO could also effectively degrade TC. However, the $\text{MgO/g-C}_3\text{N}_4$ maintained optimal PC performance. The enhanced degradation performance was attributed to the excellent optical properties and photogenerated carrier separation efficiency of the $\text{MgO/g-C}_3\text{N}_4$ S-scheme heterojunction (Fig. 5). Significantly, considering the potential of the application, actual sunlight was used as the light source for the photocatalytic degradation of TC. As shown in Fig. 7a, $\text{MgO/g-C}_3\text{N}_4$ still

exhibited a better performance (73.10%) compared with MgO and $\text{g-C}_3\text{N}_4$ in degrading TC under sunlight irradiation.

3.3.3. Synergistic effect of PC and EC in PEC system

In order to investigate the synergistic effect of PC ($\text{MgO/g-C}_3\text{N}_4$) and EC ($\text{MgO/g-C}_3\text{N}_4\text{-MCF}$) in the PEC ($\text{MgO/g-C}_3\text{N}_4\text{-MCF}$) system, the $\text{MgO/g-C}_3\text{N}_4$ photoelectrode was investigated under photolysis (only light), dark adsorption (Blank), PEC, PC and EC conditions (Fig. 7c-d). TC degradation was negligible under photolysis (only light) and dark adsorption (Blank) conditions, indicating that TC was not easily photodegraded and adsorption. As shown in Fig. 7c-d, the PEC process could completely remove TC within 30 min under LED light irradiation, which was dramatically better than previous reports (Table S3). The pseudo-first-order rate constant for the degradation of TC by the PEC process ($k = 0.1667 \text{ min}^{-1}$) was 5.3 and 1.5 times that of EC ($k = 0.0315 \text{ min}^{-1}$) and PC ($k = 0.1142 \text{ min}^{-1}$), respectively. The total organic carbon (TOC) removal of TC was about 54.59% at 2 h (Fig. S3). The results showed that the PEC system could partially mineralize TC under LED irradiation. However, compared with the PEC ($\text{MgO/g-C}_3\text{N}_4\text{-MCF}$) system, the TC degradation efficiency of the PEC ($\text{MgO/g-C}_3\text{N}_4\text{-Pt}$) system was only 88.9% after 30 min reaction, indicating that the production and activation of H_2O_2 could improve the performance of the PEC system. In addition, the remaining amount of H_2O_2 in the PEC system (1.9 mg L^{-1}) was much lower than that of EC (5.8 mg L^{-1}) with $\text{MgO/g-C}_3\text{N}_4$ anode-coupled MCF cathode (Fig. 6c). The phenomenon could be explained by the fact that $\text{MgO/g-C}_3\text{N}_4$ could produce more photoelectrons under light irradiation, which accelerated the activation of H_2O_2 to produce more ROSs to enhance the degradation efficiency of PEC. It indicated that the bias voltage could accelerate the separation of photogenerated carriers from the $\text{MgO/g-C}_3\text{N}_4$ photoanode in the PEC system, which ultimately improved the TC degradation efficiency [43]. Therefore, synergistic effects could be expected in the PEC process and

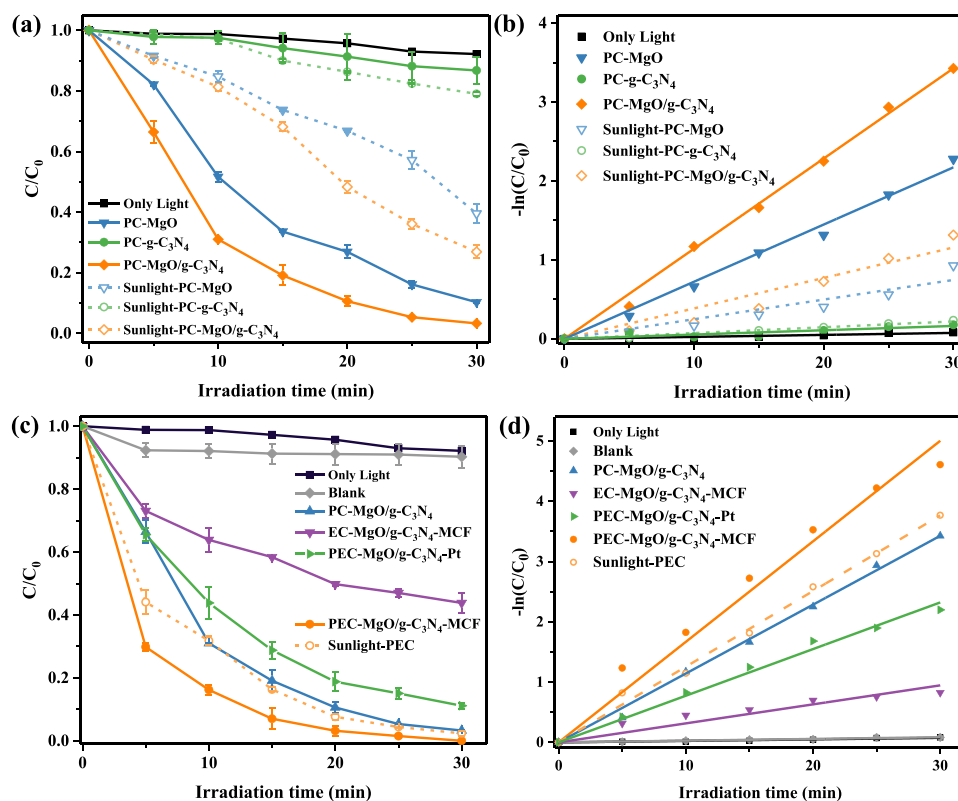


Fig. 7. (a) Degradation rate and (b) pseudo-first-order kinetic curves of TC in different PC systems, (c) degradation efficiency and (d) pseudo-first-order kinetic curves of TC in different systems. Experimental conditions: initial TC 20 mg L^{-1} , Na_2SO_4 0.1 M , pH 5.6, cathode bias -0.5 V , Sunlight-PEC system under illumination with real sunlight in winter from 11:00–15:00 (Tianjin, China).

the synergy factor (SF) was determined to be 0.14 using Eq. 1, where k_{EC} , k_{PC} and k_{PEC} represent the degradation rate constants of TC by EC, PC, and PEC processes, respectively.

$$SF = \frac{k_{PEC}}{k_{EC} + k_{PC}} - 1 \quad (1)$$

In addition, the efficiency of sunlight-PEC for TC removal reached 97.64% at 30 min under sunlight irradiation (Fig. 7c). The first-order kinetic constant of TC degradation by PEC under LED light irradiation ($k = 0.1667 \text{ min}^{-1}$) was 1.3 times that under sunlight irradiation ($k = 0.1255 \text{ min}^{-1}$). This be explained by the change in the direction of sunlight irradiation during the PEC process, which led to the insufficient utilization of sunlight by the photoanode [42]. Although the degradation efficiency of TC under sunlight illumination was slightly slower than that under LED illumination, the light density parameter under sunlight illumination (0.005 W cm^{-2} , 24°C) was much lower than that of LED (0.142 W cm^{-2} , 24°C).

3.4. Mechanism analysis

The contribution of the active species in the PEC system was evaluated by the extent to which the added sacrificial agents inhibited TC degradation. To identify the dominant reactive species towards TC removals, ammonium oxalate (AO), tert-Butanol (TBA), 1,4-benzoquinone (BQ) and furfuryl alcohol (FFA) were used as scavengers for h^+ , $\cdot\text{OH}$, $\text{O}_2^{\cdot-}$ and $^1\text{O}_2$, respectively (Fig. 8a). The degradation rate of TC significantly decreased from 100.00% to 18.30% when FFA was added to the solution, indicating that $^1\text{O}_2$ was the main active species for TC degradation (Fig. 8b). In addition, the inhibition of TC degradation was 37.57% with the addition of BQ, indicating that $\text{O}_2^{\cdot-}$ was also the main active species for degrading TC. Meanwhile, AO and TBA had a weak inhibitory effect on the MgO/g- C_3N_4 anode-coupled MCF cathode PEC

system, suggesting that h^+ and $\cdot\text{OH}$ had less effect on the degradation of TC. Therefore, the contribution of reactive species in TC degradation was in the following order: $^1\text{O}_2 > \text{O}_2^{\cdot-} > h^+ > \cdot\text{OH}$.

In order to verify the above results, electron paramagnetic resonance (EPR) technique was employed to detect the active components during TC degradation using TEMP and DMPO as spin-trapping agents, respectively. As shown in Fig. 8c, the $^1\text{O}_2$ signal of the PEC system was gradually enhanced with the reaction time, further confirming the effectiveness of the MgO/g- C_3N_4 photoanode on H_2O_2 activation activity. In addition, weak characteristic signals of DMPO- $\text{O}_2^{\cdot-}$ adducts and DMPO- $\cdot\text{OH}$ adducts appeared in the PEC system (Fig. 8d and Fig. S4). The above results indicated that the reactive oxygen generated in the PEC system was dominated by $^1\text{O}_2$, which was consistent with the results of free radical quenching experiments. Based on the structural characterization (Figs. 2 and 3) and catalytic properties (Figs. 6 and 7), the key to the activation of H_2O_2 by the MgO/g- C_3N_4 S-scheme heterojunction for TC degradation lied on the formation of electron-rich N-centers by the Mg-N coordination between MgO and g- C_3N_4 [17,20,32].

MgO and g- C_3N_4 have a staggered energy band structure, which allow the formation of conventional type II heterojunction or S-scheme heterojunction [44]. However, since the E_{VB} value of g- C_3N_4 (1.89 eV) was more negative than $\cdot\text{OH}/\text{OH}^-$ potential ($E(\cdot\text{OH}/\text{OH}^-) = 1.99 \text{ eV}$ vs. NHE) [45], which was unable to produce $\cdot\text{OH}$, and the results were inconsistent with the EPR test (Fig. S4). Therefore, it was proved that the heterojunction type was not a type II heterojunction but a S-scheme heterojunction.

In order to further investigated the heterojunction types and elucidated their mechanisms, the work functions of MgO (200) and g- C_3N_4 (002) planes with respect to the vacuum energy levels were calculated using DFT simulations based on the XRD results. From Fig. 9a-b, the work functions of MgO and g- C_3N_4 were 4.71 eV and 4.11 eV, respectively. In addition, the charge density difference at the interface of MgO

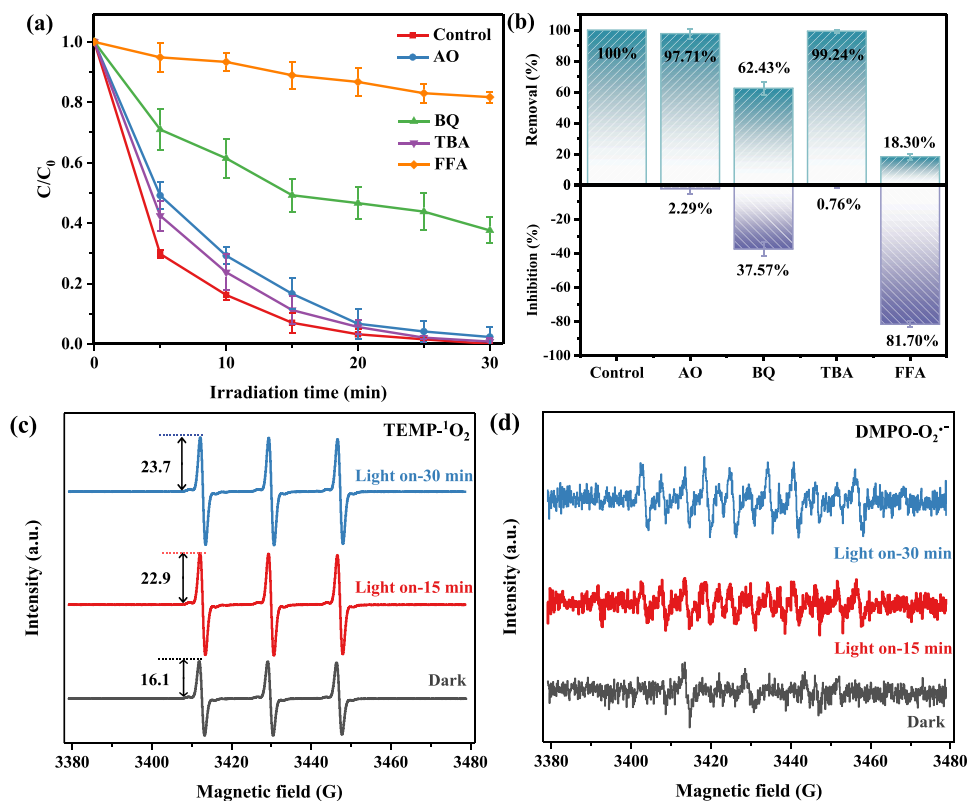


Fig. 8. (a) Effect of scavengers on the TC removal, (b) removal rate and inhibition rate of TC degradation on MgO/g- C_3N_4 photoanode with different scavenger under LED lamp irradiation. Experimental conditions: initial TC 20 mg L^{-1} , Na_2SO_4 0.1 M , pH 5.6, cathode bias -0.5 V . (c) EPR spectra of TEMP- $^1\text{O}_2$ adduct and (d) DMPO- $\text{O}_2^{\cdot-}$ adduct.

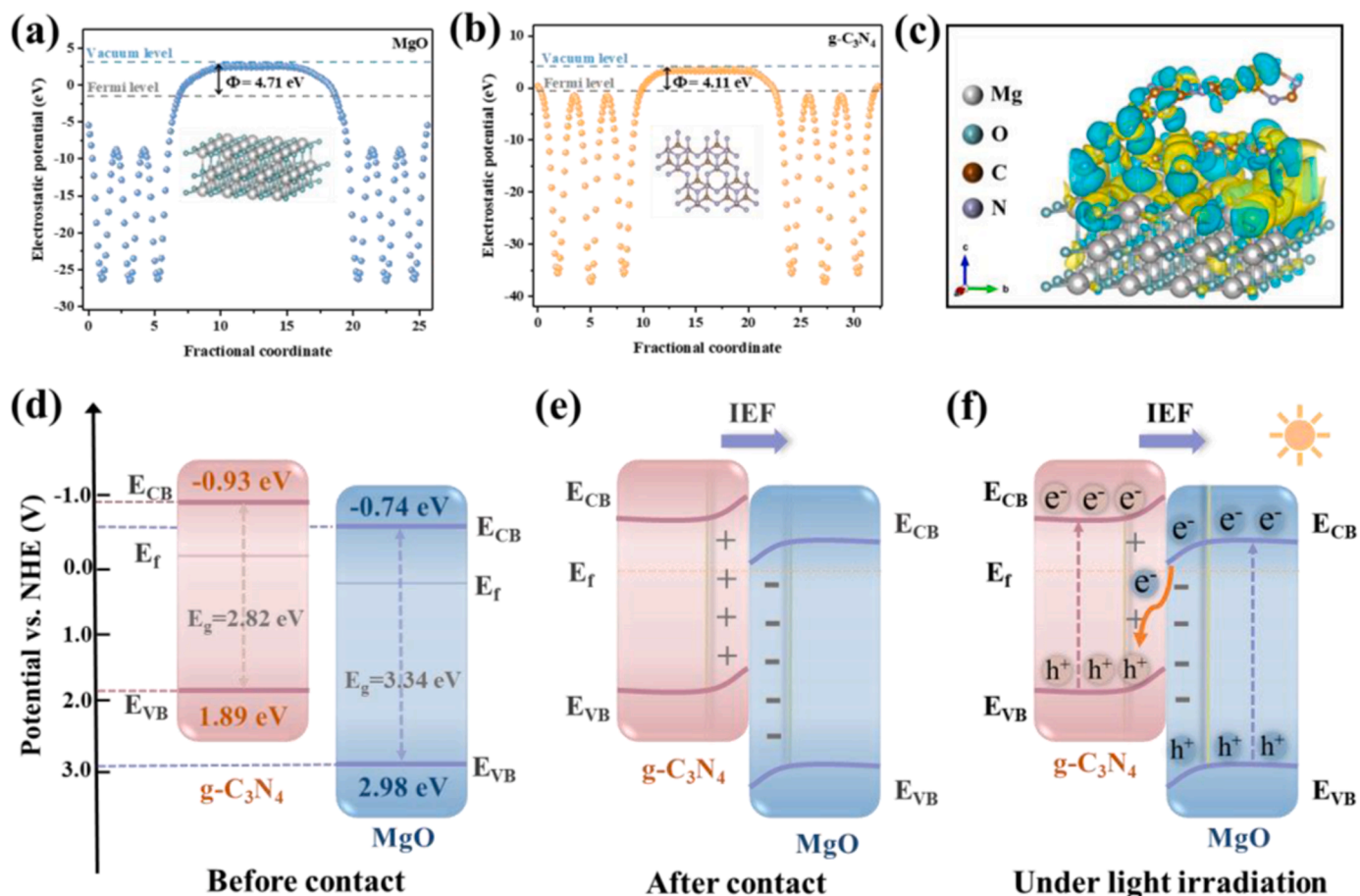


Fig. 9. Calculated the electrostatic potential for the (200) face of (a) MgO and (002) face of (b) g-C₃N₄ surfaces. The gray and blue dashed lines indicate the Fermi level and vacuum level, respectively. In the geometry structures of MgO and g-C₃N₄, the gray, green, brown, and purple spheres represent Mg, O, C, and N atoms, respectively. (c) Charge density difference at MgO/g-C₃N₄ interface, yellow means loss of electrons, and blue means gain of electrons. (d-f) Schematic illustration of MgO/g-C₃N₄ S-scheme heterojunction.

and g-C₃N₄ heterojunction was further simulated to determine the charge transfer. The results of Fig. 9c showed that g-C₃N₄ lost electrons and transferred to the MgO interface. Both sides of MgO and g-C₃N₄ had

positive and negative charges, respectively, resulting in an internal electric field at the interface.

Based on the difference in Fermi energy levels, when MgO was in

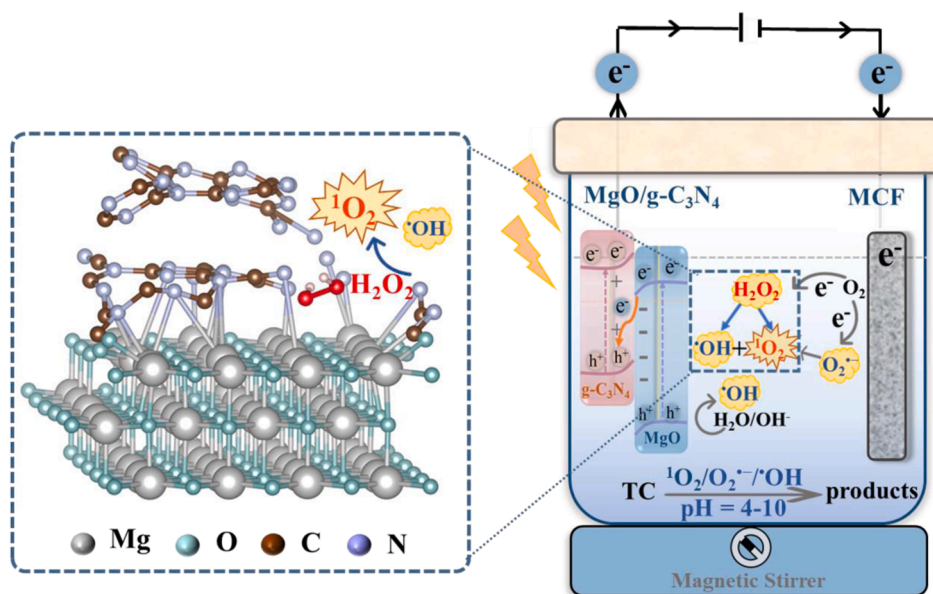
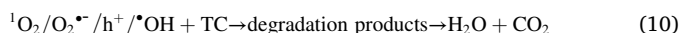
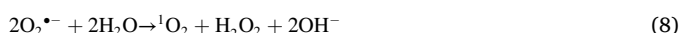


Fig. 10. The reaction mechanism of PEC degradation of TC by MgO/g-C₃N₄ photoanode coupled with MCF cathode system.

contact with g-C₃N₄ under dark conditions, electrons would spontaneously migrate from g-C₃N₄ to MgO until their Fermi energy levels reached equilibrium (Fig. 9d-e). Subsequently, more electrons would accumulate on the MgO side, forming an accumulation layer that bended the energy band downward of MgO. Some holes were left on the g-C₃N₄ side, forming a depletion layer with the band bending upward. Under light excitation, driven by the internal electric field and bent bands, the photogenerated electrons in the CB of MgO spontaneously transfer to g-C₃N₄ and combine with the holes in the VB of g-C₃N₄ (Fig. 9f). The above electron transfer results were consistent with *in-situ* irradiation XPS spectra results, further illustrating the S-scheme heterojunction structure of MgO/g-C₃N₄.

On this basis, the reaction mechanism of PEC degradation of TC by MgO/g-C₃N₄ photoanode coupled with MCF cathode system was proposed. As shown in Fig. 10, under the effect of applied voltage and S-scheme heterojunction, the electrons in the CB of g-C₃N₄ with strong reducing ability were transferred to the cathode, which improved the separation rate of electron-hole pairs (Eq. 2). In addition, the photo-generated electrons transferred to the cathode could react to generate O₂^{•−} to remove TC (Eq. 3, Eq. 10). The holes in the valence band of MgO with strong oxidizing ability in the MgO/g-C₃N₄ photoanode could oxidize OH[−]/H₂O to [•]OH (E = 1.99/2.38 eV vs. NHE) thus effectively degrading TC (Eq. 4, Eq. 10) [46]. In addition, the H₂O₂ generated by the MCF cathode could be converted to ¹O₂ and [•]OH by the catalytic activation of the MgO/g-C₃N₄ anode, which further participated in the degradation of organic pollutants (Eqs. 5–10) [17,47]. Therefore, the MgO/g-C₃N₄ photoanode coupled MCF cathode system had an efficient PEC performance under the synergistic effect of PC and EC.



3.5. Possible degradation pathway of TC and toxicity assessment

The degradation intermediates of TC were identified using LC-MS, and the mass spectra of the intermediates were shown in Fig. S5. Accordingly, we proposed three possible pathways for TC degradation, as shown in Fig. S6. For pathway I: through the oxidation of ¹O₂ and O₂^{•−}, TC (*m/z* = 445) striped off the amide group and hydroxyl group to form T2 (*m/z* = 384) [3]. T3 (*m/z* = 338) was formed from the intermediate T2 by ring opening, demethylation and addition reactions. In addition, T6 (*m/z* = 282) was formed by decarboxylation and ring opening of T3. Subsequently, T6 was further oxidized by deaminating, ring opening and dehydroxylation to form T8 (*m/z* = 214) and T10 (*m/z* = 114). Finally, T10 was oxidized to the small molecule intermediate T9 (*m/z* = 116). For pathway II: electron-rich double bonds, amide groups and dimethylamino group functionalities in TC molecules were more susceptible to attack by electrophilic ¹O₂ and [•]OH [20,48]. TC attacked by ¹O₂ and [•]OH formed T4 (*m/z* = 332) by reactions such as removal of amide groups, dimethylamino groups, ring opening and demethylation [49]. The active substance attacked the double bond and the hydroxyl

group, leaving a ketone group and forming a T7 (*m/z* = 274) compound. Eventually, T7 formed the small molecule intermediate T9 by oxidation by ¹O₂ and O₂^{•−}. For pathway III: the T1 (*m/z* = 415) intermediate was formed through the attack of the dimethylamino group of TC and the dehydroxylation reaction. Furthermore, the T1 product was stripped of its amide group, ring-opened and dehydroxylated to form T5 (*m/z* = 283), which was ultimately further oxidized to T9 by ring-opening and deamidation. Finally, these intermediates were oxidized to small molecular products (CO₂ and H₂O) by ¹O₂, O₂^{•−} and [•]OH.

The acute toxicity LC₅₀, developmental toxicity and mutagenicity of TC and degradation intermediates were further evaluated using Toxicity Evaluation Software Tool (T.E.S.T.) based on the quantitative structure-activity relationship (QSAR) mathematical model [50,51]. Acute toxicity evaluations of TC showed that the LC₅₀ of TC for fathead minnow and *Daphnia magna* was 0.90 mg L^{−1} and 12.70 mg L^{−1}, respectively, which was considered "toxic" (Fig. S7a-b). However, the hazards of the intermediates were lower than those of TC, except for intermediates T1, T2 and T5, which were slightly higher than TC. In addition, the LC₅₀-48 h values of the detected intermediates were higher than those of TC, except for intermediates T1, T2, T4 and T5, which indicated that the toxicity of the intermediates was weakened. Furthermore, T8 was harmless to fathead minnow and *Daphnia magna*. The above results indicated that the acute toxicity of TC to fathead minnow and *Daphnia magna* was effectively reduced after its degradation in the PEC system. Worryingly, in terms of the developmental toxicity of the intermediates, both TC and the intermediates were developmentally toxic, with T1, T2, T4, T7 and T8 being more developmentally toxic than TC (Fig. S7c). Besides, the mutagenicity results of TC and its intermediates showed that the intermediates had negative mutagenicity except for the intermediates T1, T3, T4 and T10 (Fig. S7d). Therefore, based on the overall toxicity prediction results, it was confirmed that the environmental hazards of TC could be mitigated during the degradation process in the PEC system.

3.6. Evaluation of the PEC system in practical applications

To evaluate the degradation performance of MgO/g-C₃N₄ anode-coupled MCF cathode system, a series of experiments were carried out under different conditions. Initially, the effect of initial solution pH on the MgO/g-C₃N₄-MCF system was investigated (Fig. 11a-b, Fig. S8a). Studies have shown that ¹O₂ has a wider pH tolerance and ¹O₂ production increases with increasing pH [52]. Therefore, the MgO/g-C₃N₄-MCF system could effectively degrade TC over a wide pH range from 4 to 10 (Fig. 11a). This system solves the problem that the Fenton/Fenton-like system is only effective in a narrow pH range (pH = 2–4) [53]. However, the degradation efficiency was only 35.68% within 30 min at an initial solution pH of 2, which may be due to the partial dissolution of MgO/g-C₃N₄ components in the solution, thus breaking the heterogeneous structure of the catalyst.

Based on the prevalence of anions and natural organic matter in real wastewater, the effects of common anions such as Cl[−], NO₃[−], CO₃^{2−}, PO₄^{3−} and natural organic matter humic acids (HA) on the degradation of TC by PEC in the MgO/g-C₃N₄-MCF system were investigated. As shown in Fig. 11c and Fig. S8b, the introduction of anions such as 10 mM Cl[−], CO₃^{2−}, NO₃[−], and PO₄^{3−} had only a slight effect on TC degradation, indicating that the PEC system was highly resistant to the above common anions. Based on the background composition of the actual water environment, the concentration of HA introduced into the system was 10 mg L^{−1} [42]. As shown in Fig. 11c, HA would compete with TC for active radicals due to its degradability, resulting in a slight decrease in TC degradation efficiency, but TC degradation could still reach 94.00%. The above results indicated that the MgO/g-C₃N₄-MCF PEC system had high adaptability in practical wastewater purification.

In addition, water sources with different water qualities, such as tap water, lake water, mariculture water and pharmaceutical water were used to prepare TC reaction solutions, respectively (See Table S4 for

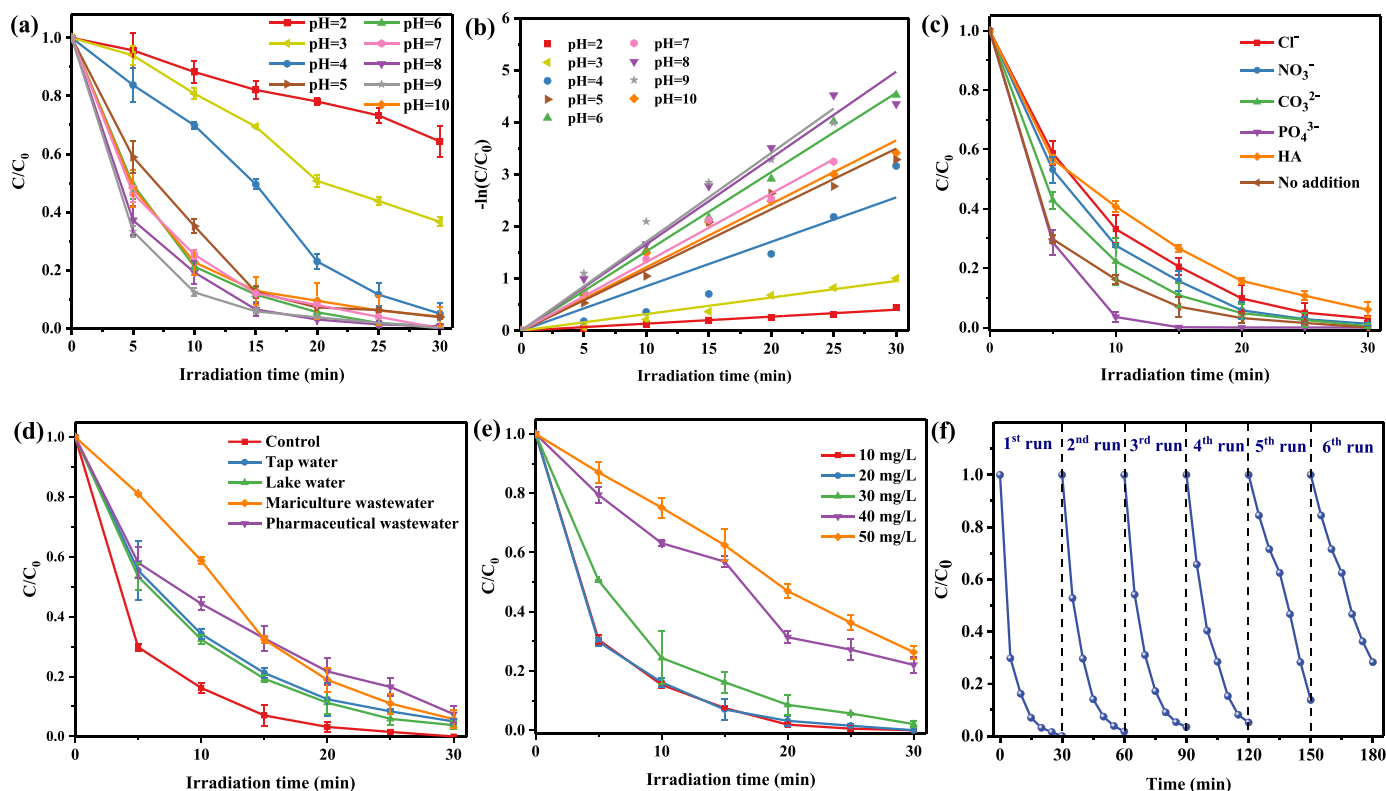


Fig. 11. Influence factors of TC degradation by PEC in MgO/g-C₃N₄ photoanode-coupled MCF cathode system within 30 min: (a) initial solution pH and (b) pseudo-first-order kinetic curves, (c) co-existing anions, (d) water source, (e) initial TC concentration. (f) Recycling tests of TC degradation by PEC in MgO/g-C₃N₄ anode-coupled MCF cathode system, experimental conditions: initial TC 20 mg L⁻¹, Na₂SO₄ 0.1 M, pH 5.6, cathode bias -0.5 V.

water quality parameters). As shown in Fig. 11d, although the presence of different organic matter, inorganic matter and microorganisms in the above water sources would deplete the active substances produced by the PEC system, it had little effect on the PEC degradation of TC. The experimental results showed that the efficiency of PEC degradation of TC all still reached more than 90% within 30 min. The possible reason was that the PEC system was dominated by non-free radical pathway based on ¹O₂, which was resistant to common background substances in water matrix. Therefore, the above analysis proved that the MgO/g-C₃N₄-MCF system had the potential for TC degradation by PEC in different water matrices.

In addition, the effects of different initial concentrations of TC (10 mg L⁻¹ - 50 mg L⁻¹) solutions on PEC degradation were shown in Fig. 11e. With the increase of the initial concentration, the efficiency gradually decreased. In fact, during the PEC degradation process, the high concentration of TC would have more intermediates, which made the TC obtain limited active sites and active radicals. In addition, the higher initial pollutant concentration would hinder the penetration of light into the reaction solution, resulting in a reduction of effective photons [54].

The stability of the photoanode and cathode in the PEC system is crucial for further applications. Therefore, the reusability and stability of MgO/g-C₃N₄-MCF were also investigated. As shown in Fig. 11f, the removal of TC was 100.00%, 98.28%, 96.57%, 94.81%, 86.22%, and 71.74% for six cycling experiments, remaining at a high level during first four cycling experiments. The degradation performance of the PEC decreased with the number of electrode usage, probably due to the limited coordination of MgO and g-C₃N₄ in the MgO/g-C₃N₄ photoanode, which led to the reduced activity [28]. However, the overall performance showed that the PEC system had high stability. In addition, XRD of fresh samples and reused samples showed that the peak of MgO in MgO/g-C₃N₄ was weakened, and heterostructure construction of MgO and g-C₃N₄ were partially limited, resulting in a decrease in the

reutilization activity of the photoanode (Fig. S9a). The XPS results of fresh and used photoanodes showed that the structure of the photoanodes did not change significantly (Fig. S9b-d). In addition, as can be seen in Fig. S9e-f, the surface of the photoanode became rougher after six cycles of testing, and MgO partially aggregated, which may lead to the degradation of the performance of the photoanode. Moreover, with the degradation of TC by PEC, a small amount of Mg²⁺ in MgO/g-C₃N₄ was leaching, which may be one of the reasons for the decline in photoanode activity (Fig. S10).

In addition, methylene blue, orange G, phenol and sulfamethazine were used as target contaminants to verify the universality of the PEC process. Fig. S11 showed that the removal rates of methylene blue and orange G in the PEC system reach 98.2% and 80.5% within 90 min, respectively, and the removal of phenol and sulfamethazine reached 63.1% and 98.5% within 240 min. The results presented that the PEC system possessed the enhanced performance for degradation of different pollutants.

4. Conclusions

In summary, MgO/g-C₃N₄ S-scheme heterojunction photoanode were successfully prepared which possessed both excellent photocatalytic performance and H₂O₂ activation, and a PEC system with this bifunctional photoanode and MCF cathode was constructed. After 30 min of LED irradiation, the PEC system could completely remove TC at a cathode bias of -0.5 V (vs. Ag/AgCl), obtaining a synergy with EC and PC. Quenching experiments and EPR test results showed that the main ROSs in the PEC system were ¹O₂ and O₂^{•-}. Furthermore, DFT calculations demonstrated that the construction of the MgO/g-C₃N₄ S-scheme heterojunction and the formation of the internal electric field effectively, and MgO/g-C₃N₄ photoanode was more favorable for H₂O₂ adsorption. Thereby, the photogenerated carrier complexation was effectively suppressed and the PEC performance of the photoanode was

improved. In addition, the PEC system had the potential for practical application, achieving 98.12% TC removal at 30 min while utilizing sunlight instead of LED light source. The PEC system had excellent TC degradation performance at a wide pH (4–10). Moreover, the degradation intermediates were identified by LC-MS and a possible PEC degradation pathway for TC was proposed. This study provides a feasible way to construct double-function S-scheme heterojunction, and proposes a new idea for the treatment of wastewater by PEC process under actual sunlight.

CRedit authorship contribution statement

Jiangli Sun: Writing – original draft, Validation, Software, Methodology, Investigation, Formal analysis, Data curation. **Minghua Zhou:** Writing – review & editing, Validation, Project administration, Methodology, Funding acquisition, Formal analysis, Conceptualization. **Chunhong Fu:** Visualization, Validation. **Huizhong Wu:** Validation, Software. **Zhongzheng Hu:** Validation, Methodology. **Chaohui Zhang:** Validation, Software.

Declaration of Competing Interest

The authors declare that they have no known competing financial interests or personal relationships that could have appeared to influence the work reported in this paper.

Data availability

Data will be made available on request.

Acknowledgments

This work was financially supported by National Key R&D Program International Cooperation Project (2023YFE0108100), Key Project of Natural Science Foundation of Tianjin (no. 21JCZDJJC00320), and Fundamental Research Funds for the Central Universities, Nankai University.

Appendix A. Supporting information

Supplementary data associated with this article can be found in the online version at [doi:10.1016/j.apcatb.2024.123976](https://doi.org/10.1016/j.apcatb.2024.123976).

References

- [1] Z. Guo, F. Yang, R. Yang, L. Sun, Y. Li, J. Xu, Preparation of novel ZnO-NP@Zn-MOF-74 composites for simultaneous removal of copper and tetracycline from aqueous solution, *Sep. Purif. Technol.* 274 (2021) 118949, <https://doi.org/10.1016/j.seppur.2021.118949>.
- [2] N. Li, L. Zhou, X. Jin, G. Owens, Z. Chen, Simultaneous removal of tetracycline and oxytetracycline antibiotics from wastewater using a ZIF-8 metal organic-framework, *J. Hazard. Mater.* 366 (2019) 563–572, <https://doi.org/10.1016/j.jhazmat.2018.12.047>.
- [3] X. Gao, J. Niu, Y. Wang, Y. Ji, Y. Zhang, Solar photocatalytic abatement of tetracycline over phosphate oxoanion decorated Bi₂WO₆/polyimide composites, *J. Hazard. Mater.* 403 (2021) 123860, <https://doi.org/10.1016/j.jhazmat.2020.123860>.
- [4] Y. Li, B. Yu, Z. Hu, H. Wang, Construction of direct Z-scheme SnS₂@ZnIn₂S₄@kaolinite heterostructure photocatalyst for efficient photocatalytic degradation of tetracycline hydrochloride, *Chem. Eng. J.* 429 (2022) 132105, <https://doi.org/10.1016/j.cej.2021.132105>.
- [5] J. Qu, D. Zhang, Y. Li, P. Wang, Y. Mao, T. Zhang, S. Zhan, Y. Li, In situ synthesized S-type heterojunction Bi₂O₃/CuBi₂O₄ enable efficient NIR light-driven H₂O₂ activation for water purification, *Appl. Catal. B: Environ.* 340 (2024) 123246, <https://doi.org/10.1016/j.apcatb.2023.123246>.
- [6] Q. Zhang, M. Zhou, Z. Lang, X. Du, J. Cai, L. Han, Dual strategies to enhance mineralization efficiency in innovative electrochemical advanced oxidation processes using natural air diffusion electrode: Improving both H₂O₂ production and utilization efficiency, *Chem. Eng. J.* 413 (2021) 127564, <https://doi.org/10.1016/j.cej.2020.127564>.
- [7] S. Li, J. Xie, J. Gu, M. Zhou, Hybrid peroxi-coagulation/ozonation process for highly efficient removal of organic contaminants, *Chin. Chem. Lett.* (2023) 108204, <https://doi.org/10.1016/j.ccl.2023.108204>.
- [8] J. Sun, Y. Hou, Z. Yu, L. Tu, Y. Yan, S. Qin, S. Chen, D. Lan, H. Zhu, S. Wang, Visible-light-driven Z-scheme Zn₃In₂S₆/AgBr photocatalyst for boosting simultaneous Cr (VI) reduction and metronidazole oxidation: kinetics, degradation pathways and mechanism, *J. Hazard. Mater.* 419 (2021) 126543, <https://doi.org/10.1016/j.jhazmat.2021.126543>.
- [9] G. Song, X. Du, Y. Zheng, P. Su, Y. Tang, M. Zhou, A novel electro-Fenton process coupled with sulfite: enhanced Fe³⁺ reduction and TOC removal, *J. Hazard. Mater.* 422 (2022) 126888, <https://doi.org/10.1016/j.jhazmat.2021.126888>.
- [10] J. Guo, G. Song, Y. Zheng, J. Gu, S. Li, M. Zhou, Single iron atoms embedded in MOF-derived nitrogen-doped carbon as an efficient heterogeneous electro-Fenton catalyst for degradation of carbamazepine over a wide pH, *Sep. Purif. Technol.* 302 (2022) 122141, <https://doi.org/10.1016/j.seppur.2022.122141>.
- [11] H. Wu, Z. Hu, R. Liang, O.V. Nkwachukwu, O.A. Arotiba, M. Zhou, Novel Bi₂Sn₂O₇ quantum dots/TiO₂ nanotube arrays S-scheme heterojunction for enhanced photoelectrocatalytic degradation of sulfamethazine, *Appl. Catal. B: Environ.* 321 (2023) 122053, <https://doi.org/10.1016/j.apcatb.2022.122053>.
- [12] J. Wang, Z. Wang, K. Dai, J. Zhang, Review on inorganic-organic S-scheme photocatalysts, *J. Mater. Sci. Technol.* 165 (2023) 187–218, <https://doi.org/10.1016/j.jmst.2023.03.067>.
- [13] H. Sun, P. Qin, J. Guo, Y. Jiang, Y. Liang, X. Gong, X. Ma, Q. Wu, J. Zhang, L. Luo, Z. Wu, Enhanced electron channel via the interfacial heterotropic electric field in dual S-scheme g-C₃N₄/WO₃/ZnS photocatalyst for year-round antibiotic degradation under sunlight, *Chem. Eng. J.* 470 (2023) 144217, <https://doi.org/10.1016/j.cej.2023.144217>.
- [14] J. Wang, G. Wang, B. Cheng, J. Yu, J. Fan, Sulfur-doped g-C₃N₄/TiO₂ S-scheme heterojunction photocatalyst for Congo Red photodegradation, *Chin. J. Catal.* 42 (2021) 56–68, [https://doi.org/10.1016/s1872-2067\(20\)63634-8](https://doi.org/10.1016/s1872-2067(20)63634-8).
- [15] X. An, X. Xu, W. Guo, Z. Chen, Z. Miao, J. Yuan, Z. Wu, Bi-functional biochar-g-C₃N₄-MgO composites for simultaneously minimizing pollution: photocatalytic degradation of pesticide and phosphorus recovery as slow-release fertilizer, *J. Environ. Manag.* 344 (2023) 118489, <https://doi.org/10.1016/j.jenvman.2023.118489>.
- [16] A. Modwi, L. Khezami, M.G. Ghoniem, P. Nguyen-Tri, O. Baaloudj, A. Guesmi, F. K. Algethami, M.S. Amer, A.A. Assadi, Superior removal of dyes by mesoporous MgO/g-C₃N₄ fabricated through ultrasound method: adsorption mechanism and process modeling, *Environ. Res.* 205 (2022) 112543, <https://doi.org/10.1016/j.envres.2021.112543>.
- [17] T. Li, L. Ge, X. Peng, W. Wang, W. Zhang, Enhanced degradation of sulfamethoxazole by a novel Fenton-like system with significantly reduced consumption of H₂O₂ activated by g-C₃N₄/MgO composite, *Water Res.* 190 (2021) 116777, <https://doi.org/10.1016/j.watres.2020.116777>.
- [18] P.V.R.K. Ramacharyulu, S.J. Abbas, S.R. Sahoo, S.-C. Ke, Mechanistic insights into 4-nitrophenol degradation and benzyl alcohol oxidation pathways over MgO/g-C₃N₄ model catalyst systems, *Catal. Sci. Technol.* 8 (2018) 2825–2834, <https://doi.org/10.1039/c8cy00431e>.
- [19] J. Xu, Y. Chen, D. Ma, J.-K. Shang, Y.-X. Li, Simple preparation of MgO/g-C₃N₄ catalyst and its application for catalytic synthesis of dimethyl carbonate via transesterification, *Catal. Commun.* 95 (2017) 72–76, <https://doi.org/10.1016/j.catcom.2017.03.009>.
- [20] L. Ge, Y. Yue, W. Wang, F. Tan, S. Zhang, X. Wang, X. Qiao, P.K. Wong, Efficient degradation of tetracycline in wide pH range using MgCN/MgO nanocomposites as novel H₂O₂ activator, *Water Res.* 198 (2021) 117149, <https://doi.org/10.1016/j.watres.2021.117149>.
- [21] M. Gao, Z. Li, X. Su, X. Zhang, J. Chang, D. Geng, Y. Lu, H. Zhang, T. Wei, J. Feng, 2D/2D MgO/g-C₃N₄ S-scheme heterogeneous tight with Mg–N bonds for efficient photo-Fenton degradation: enhancing both oxygen vacancy and charge migration, *Chemosphere* 343 (2023) 140285, <https://doi.org/10.1016/j.chemosphere.2023.140285>.
- [22] P. Su, M. Zhou, X. Lu, W. Yang, G. Ren, J. Cai, Electrochemical catalytic mechanism of N-doped graphene for enhanced H₂O₂ yield and in-situ degradation of organic pollutant, *Appl. Catal. B: Environ.* 245 (2019) 583–595, <https://doi.org/10.1016/j.apcatb.2018.12.075>.
- [23] J. Jing, X. Wang, M. Zhou, Electro-enhanced activation of peroxydisulfate by a novel perovskite-TiO₂ composite anode with ultra-high efficiency and low energy consumption: The generation and dominant role of singlet oxygen, *Water Res.* 232 (2023) 119682, <https://doi.org/10.1016/j.watres.2023.119682>.
- [24] Y. Wang, L. Rao, P. Wang, Z. Shi, L. Zhang, Photocatalytic activity of N-TiO₂/O-doped N vacancy g-C₃N₄ and the intermediates toxicity evaluation under tetracycline hydrochloride and Cr(VI) coexistence environment, *Appl. Catal. B: Environ.* 262 (2020) 118308, <https://doi.org/10.1016/j.apcatb.2019.118308>.
- [25] G. Kresse, J. Furthmüller, Efficient iterative schemes for ab initio total-energy calculations using a plane-wave basis set, *Phys. Rev. B* 54 (1996) 11169, <https://doi.org/10.1103/PhysRevB.54.11169>.
- [26] G. Kresse, J. Furthmüller, Efficiency of ab-initio total energy calculations for metals and semiconductors using a plane-wave basis set, *Comput. Mater. Sci.* 6 (1996) 15–50, [https://doi.org/10.1016/0927-0256\(96\)00008-0](https://doi.org/10.1016/0927-0256(96)00008-0).
- [27] J.P. Perdew, K. Burke, M. Ernzerhof, Generalized gradient approximation made simple, *Phys. Rev. Lett.* 78 (1997) 1396, <https://doi.org/10.1103/physrevlett.77.3865>.
- [28] L. Ge, Z. Peng, W. Wang, F. Tan, X. Wang, B. Su, X. Qiao, P.K. Wong, g-C₃N₄/MgO nanosheets: light-independent, metal-poisoning-free catalysts for the activation of hydrogen peroxide to degrade organics, *J. Mater. Chem. A* 6 (2018) 16421–16429, <https://doi.org/10.1039/c8ta05488f>.

- [29] J. Madona, C. Sridevi, Surfactant assisted hydrothermal synthesis of MgO/g-C₃N₄ heterojunction nanocomposite for enhanced solar photocatalysis and antimicrobial activities, *Inorg. Chem. Commun.* 138 (2022) 109265, <https://doi.org/10.1016/j.inoche.2022.109265>.
- [30] W. An, L. Tian, J. Hu, L. Liu, W. Cui, Y. Liang, Efficient degradation of organic pollutants by catalytic ozonation and photocatalysis synergy system using double-functional MgO/g-C₃N₄ catalyst, *Appl. Surf. Sci.* 534 (2020) 147518, <https://doi.org/10.1016/j.apsusc.2020.147518>.
- [31] N. Dong, D. Wu, L. Ge, W. Wang, F. Tan, X. Wang, X. Qiao, P.K. Wong, Constructing a brand-new advanced oxidation process system composed of MgO₂ nanoparticles and MgNCN/MgO nanocomposites for organic pollutant degradation, *Environ. Sci.: Nano* 9 (2022) 335–348, <https://doi.org/10.1039/d1en00751c>.
- [32] N. Dong, L. Ge, P. Chen, W. Wang, F. Tan, X. Wang, X. Qiao, P. Keung Wong, Non-radical activation of CaO₂ nanoparticles by MgNCN/MgO composites for efficient remediation of organic and heavy metal-contaminated wastewater, *Sep. Purif. Technol.* 285 (2022) 120334, <https://doi.org/10.1016/j.seppur.2021.120334>.
- [33] N. Mao, J.-X. Jiang, MgO/g-C₃N₄ nanocomposites as efficient water splitting photocatalysts under visible light irradiation, *Appl. Surf. Sci.* 476 (2019) 144–150, <https://doi.org/10.1016/j.apsusc.2019.01.049>.
- [34] L. Zhang, J. Zhang, H. Yu, J. Yu, Emerging S-scheme photocatalyst, *Adv. Mater.* 34 (2022) 2107668, <https://doi.org/10.1002/adma.202107668>.
- [35] Y. Chen, L. Liu, L. Zhang, S. Li, X. Zhang, W. Yu, F. Wang, W. Xue, H. Wang, Z. Bian, Construction of Z-type heterojunction BiVO₄/Sm/α-Fe₂O₃ photoanode for selective degradation: efficient removal of bisphenol A based on multifunctional Sm-doped modification, *Appl. Catal. B: Environ.* 333 (2023) 122775, <https://doi.org/10.1016/j.apcatb.2023.122775>.
- [36] F. Li, X. Li, S. Tong, J. Wu, T. Zhou, Y. Liu, J. Zhang, S-scheme heterojunction Cu₂V₂O₇/α-Fe₂O₃ nanosheets with effective photocatalytic activity toward organic pollutant degradation, *Nano Energy* 117 (2023) 108849, <https://doi.org/10.1016/j.nanoen.2023.108849>.
- [37] J. Zhu, Q. Bi, Y. Tao, W. Guo, J. Fan, Y. Min, G. Li, Mo-Modified ZnIn₂S₄@NiTiO₃ S-scheme heterojunction with enhanced interfacial electric field for efficient visible-light-driven hydrogen evolution, *Adv. Funct. Mater.* 33 (2023) 2213131, <https://doi.org/10.1002/adfm.202213131>.
- [38] F.-Z. Chen, Y.-J. Li, M. Zhou, X.-X. Gong, Y. Gao, G. Cheng, S.-B. Ren, D.-M. Han, Smart multifunctional direct Z-scheme In₂S₃@PCN-224 heterojunction for simultaneous detection and photodegradation towards antibiotic pollutants, *Appl. Catal. B: Environ.* 328 (2023) 122517, <https://doi.org/10.1016/j.apcatb.2023.122517>.
- [39] Y. Hu, X. Hao, Z. Cui, J. Zhou, S. Chu, Y. Wang, Z. Zou, Enhanced photocarrier separation in conjugated polymer engineered CdS for direct Z-scheme photocatalytic hydrogen evolution, *Appl. Catal. B: Environ.* 260 (2020) 118131, <https://doi.org/10.1016/j.apcatb.2019.118131>.
- [40] G. Jia, Y. Wang, X. Cui, Z. Yang, L. Liu, H. Zhang, Q. Wu, L. Zheng, W. Zheng, Asymmetric embedded benzene ring enhances charge transfer of carbon nitride for photocatalytic hydrogen generation, *Appl. Catal. B: Environ.* 258 (2019) 117959, <https://doi.org/10.1016/j.apcatb.2019.117959>.
- [41] Q. Zhang, F. Yang, S. Zhou, N. Bao, Z. Xu, M. Chaker, D. Ma, Broadband photocatalysts enabled by 0D/2D heterojunctions of near-infrared quantum dots/graphitic carbon nitride nanosheets, *Appl. Catal. B: Environ.* 270 (2020) 118879, <https://doi.org/10.1016/j.apcatb.2020.118879>.
- [42] Z. Hu, M. Zhou, H.A. Maitlo, R. Liang, Y. Zheng, H. Wu, X. Song, O.A. Arotiba, Novel dual-photoelectrode photoelectrocatalytic system based on TiO₂ nanoneedle arrays photoanode and nitrogen-doped carbon dots/Co₃O₄ photocathode for efficient water purification at low/no applied voltage, *Appl. Catal. B: Environ.* 331 (2023) 122676, <https://doi.org/10.1016/j.apcatb.2023.122676>.
- [43] R. Liang, Z. Hu, H. Wu, S. Li, X. Zhang, O.A. Arotiba, M. Zhou, Ti³⁺ self-doped and nitrogen-annealed TiO₂ nanocone arrays photoanode for efficient visible-LED-light-driven photoelectrocatalytic degradation of sulfamethazine, *Sep. Purif. Technol.* 314 (2023) 123591, <https://doi.org/10.1016/j.seppur.2023.123591>.
- [44] J. Sun, J. Yang, J. Liang, L. Tu, Y. Bin, Y. Hou, Construction of microspherical flower-like Zn₃In₂S₆-BGQDs/AgBr S-scheme heterojunction for photocatalytic elimination of nitrofurazone and Cr (VI), *Sep. Purif. Technol.* 299 (2022) 121563, <https://doi.org/10.1016/j.seppur.2022.121563>.
- [45] Z. Zhang, R. Ji, Q. Sun, J. He, D. Chen, N. Li, H. Li, A. Marcomini, Q. Xu, J. Lu, Enhanced photocatalytic degradation of 2-chlorophenol over Z-scheme heterojunction of CdS-decorated oxygen-doped g-C₃N₄ under visible-light, *Appl. Catal. B: Environ.* 324 (2023) 122276, <https://doi.org/10.1016/j.apcatb.2022.122276>.
- [46] H. Lu, X. Li, S.A. Monny, Z. Wang, L. Wang, Photoelectrocatalytic hydrogen peroxide production based on transition-metal-oxide semiconductors, *Chin. J. Catal.* 43 (2022) 1204–1215, [https://doi.org/10.1016/s1872-2067\(21\)64028-7](https://doi.org/10.1016/s1872-2067(21)64028-7).
- [47] Z. Jiang, J. Zhao, C. Li, Q. Liao, R. Xiao, W. Yang, Strong synergistic effect of Co₃O₄ encapsulated in nitrogen-doped carbon nanotubes on the nonradical-dominated persulfate activation, *Carbon* 158 (2020) 172–183, <https://doi.org/10.1016/j.carbon.2019.11.066>.
- [48] H. Wang, T. Chen, D. Chen, X. Zou, M. Li, F. Huang, F. Sun, C. Wang, D. Shu, H. Liu, Sulfurized oolitic hematite as a heterogeneous Fenton-like catalyst for tetracycline antibiotic degradation, *Appl. Catal. B: Environ.* 260 (2020) 118203, <https://doi.org/10.1016/j.apcatb.2019.118203>.
- [49] Z. Du, L. Feng, Z. Guo, T. Yan, Q. Hu, J. Lin, Y. Huang, C. Tang, Y. Fang, Ultrathin h-BN/Bi₂MoO₆ heterojunction with synergetic effect for visible-light photocatalytic tetracycline degradation, *J. Colloid Interface Sci.* 589 (2021) 545–555, <https://doi.org/10.1016/j.jcis.2021.01.027>.
- [50] K. Cheng, Z. Cai, J. Fu, X. Sun, W. Sun, L. Chen, D. Zhang, W. Liu, Synergistic adsorption of Cu(II) and photocatalytic degradation of phenanthrene by a jaboticaba-like TiO₂/titanate nanotube composite: An experimental and theoretical study, *Chem. Eng. J.* 358 (2019) 1155–1165, <https://doi.org/10.1016/j.cej.2018.10.114>.
- [51] C. Ling, S. Wu, J. Han, T. Dong, C. Zhu, X. Li, L. Xu, Y. Zhang, M. Zhou, Y. Pan, Sulfide-modified zero-valent iron activated periodate for sulfadiazine removal: Performance and dominant routine of reactive species production, *Water Res.* 220 (2022) 118676, <https://doi.org/10.1016/j.watres.2022.118676>.
- [52] P. Su, W. Fu, Z. Hu, J. Jing, M. Zhou, Insights into transition metal encapsulated N-doped CNTs cathode for self-sufficient electrocatalytic degradation, *Appl. Catal. B: Environ.* 313 (2022) 121457, <https://doi.org/10.1016/j.apcatb.2022.121457>.
- [53] P. Cao, K. Zhao, X. Quan, S. Chen, H. Yu, Efficient and stable heterogeneous electro-Fenton system using iron oxides embedded in Cu, N co-doped hollow porous carbon as functional electrocatalyst, *Sep. Purif. Technol.* 238 (2020) 116424, <https://doi.org/10.1016/j.seppur.2019.116424>.
- [54] L. Li, C.-G. Niu, H. Guo, J. Wang, M. Ruan, L. Zhang, C. Liang, H.-Y. Liu, Y.-Y. Yang, Efficient degradation of Levofloxacin with magnetically separable ZnFe₂O₄/NCDs/Ag₂CO₃ Z-scheme heterojunction photocatalyst: Vis-NIR light response ability and mechanism insight, *Chem. Eng. J.* 383 (2020) 123192, <https://doi.org/10.1016/j.cej.2019.123192>.